Charge transfer photodynamics in halogen doped xenon matrices. II. Photoinduced harpooning and the delocalized charge transfer states of solid xenon halides (F, Cl, Br, I)

Mario E. Fajardo and V. A. Apkarian
Department of Chemistry, University of California, Irvine, California 92717

(Received 29 April 1988; accepted 24 June 1988)

The optically accessed charge transfer states of solid xenon doped with atomic halogens are excitonic in nature: an electron localized on the guest halogen atom and a delocalized hole centered on xenon atoms. These excitonic states are effectively self-trapped such that luminescence is observed exclusively from the localized molecular charge transfer states: the triatomic xenon halide exciplexes. The latter relax radiatively. The emission spectra of $Xe_2^+ I^-$, $Xe_2^+ Br^-$, $Xe_2^+ Cl^-$, and $Xe_2^+ F^-$ are centered at 390, 480, 573, and 775 nm, and their radiative lifetimes are 130, 185, 225, and 190 ns, respectively. The charge transfer excitation spectra of the atomic solids are presented. In the case of F doped solids, the vertical transitions correspond to the diatomic XeF ($B \leftarrow X$) and ($D \leftarrow X$) absorptions: fluorine is bound to xenon in the ground state. The heavier halogens isolate atomically. Their excitation spectra are treated by a modified reflection approximation: reflection of the halogen–xenon radial distribution function from the hole transport potential. Ion–hole pairs separated by many lattice sites can be created by optical excitation, hence the spectra yield both the long range hole transport potential and the extended structure of the solid around the impurity site. The structure is fcc. Cl atoms generated by photodissociation of HCl or Cl_2 are born at interstitial sites and convert to substitutional upon annealing of the solids. The atomic solids are prepared by two-photon induced harpoon reactions between xenon and molecular halogens: $Xe + X_2 + 2h\nu \rightarrow [Xe^+X_2^-] \rightarrow Xe^+X^- + X$. The inordinate efficiency of these reactions are attributed to the ionic potentials and the intimate participation of the polarizable cage atoms in ejecting the neutral halogen—a "negative" cage effect is postulated.

I. INTRODUCTION

This paper is the second in a series dedicated to studies of charge transfer (CT) photodynamics in doped rare gas solids (RGS). In the first paper,[1] herein referred to as I, we discussed the condensed phase, photoinduced charge transfer reactions between molecular halogens (Cl_2 and HCl) and xenon, in the context of cooperative photodynamics[2]; and we assigned the emissions of the chemiluminescent products to the localized charge transfer complexes: the molecular Xe^+Cl^- and $Xe_2^+ Cl^-$ exciplexes. This assignment refers to the relaxed charge transfer states of the solid since it was based on the analysis of emission spectra that are collected on the time scale of radiative lifetimes of $\sim 10^{-7}$ s. The main objective of the present report is the spectroscopic analysis of the delocalized CT states of solid xenon doped with atomic halogens (F, Cl, Br, and I). Here we are concerned with the optically accessed CT states prior to relaxation, and the analysis will be based on excitation spectra. A secondary aim is the extension of principles developed in I, photoinduced harpooning and the spectroscopy of localized exciplexes, to the entire family of halogens isolated in solid xenon matrices. The dynamical consequences of the coexistence of both localized and delocalized CT states in these atomic solids (charge separation, self-trapping, energy storage, tunneling, and thermally induced ion–hole recombination) will be taken up in the following paper.

A. Photoinduced harpooning

Two-photon induced charge transfer reactions in both transient,[3] and jet cooled[4] complexes of xenon and molecular halogens (X_2) have been characterized in some depth in the gas phase. The process can be regarded as the photoinduced analog of the classic harpoon reactions:

$$Xe\cdots X_2 + 2h\nu \rightarrow [Xe^+X_2^-] \rightarrow Xe^+X^- + X. \qquad (1)$$

That these processes are efficient in the solid state and lead to the permanent dissociation of Cl_2 and HCl was demonstrated in I. In the present study, this charge transfer reaction is used as a method for preparing atomic halogens (F, Cl, Br, and I) in solid xenon—in effect implying a general efficiency of these ionic reactions in condensed media. Clearly Eq. (1) is an oversimplification of the condensed phase dynamics since it fails to represent the many-body nature, with respect to both electronic and nuclear coordinates, of these processes. Nevertheless, the framework of photoinduced harpooning has proven a useful paradigm for the unraveling of microscopic dynamics in condensed phases—in both solid[5] and liquid rare gases.[6] This adaptation was recently presented in a general overview article.[7] These reactions proceed via ionic potentials which, due to their long range nature, will intimately involve solvent atoms. While the description of the ionic hypersurfaces and the associated dynamics represents a challenge to both theory and experiment, their pur-

 0021-9606/88/194102-22$02.10

suit is well deserved since they are arguably most pertinent to *chemistry* in dense media.[7] The permanent dissociation of small molecules isolated in matrices is a case in point. In the series of studies on Cl_2,[8] ICl,[9] Br_2,[10] and methyl iodides[11] doped matrices, Bondybey, Brus and co-workers, have firmly established that photodissociation is prevented by a nearly complete cage effect when molecular dissociative coordinates are accessed optically. In the first report on matrix isolated exciplexes, Andrews and Ault had to resort to special techniques to generate atomic halogens, and the *in situ* photolysis of Br_2 proved to be nearly impossible.[12] In recent molecular dynamics simulations of HI photodissociation in crystalline xenon, it has been graphically demonstrated that even the ejection of an H atom is subject to a large cage effect.[13] These principles have been verified in our laboratory and can be well traced in the matrix literature. Yet, the permanent dissociation of molecular halogens and hydrogen halides via ionic potentials will be shown to proceed with great facility.

The characterization of optical resonances and cross sections of the photoinduced harpoon reaction of Eq. (1) has proven to be difficult in solid matrices. The difficulty stems from two main reasons: first the charge transfer resonances of the reagents are inherently broad; second the reaction is accompanied by efficient atomization of guests, the resulting atomic charge transfer absorptions of which are very broad and intense, and hence mask the reagent state resonances. The first of these considerations has been discussed, and the thresholds of the CT absorptions have been reported in studies of X_2:Xe liquid solutions ($X_2 = F_2$, Cl_2, Br_2).[14] The second consideration, while useful for the preparation of atomic halogens, represents an experimental difficulty in probing reagent state properties. In a static volume of interrogation, when chemistry occurs, both reagent and product states are probed simultaneously. Information about the initial state dynamics can only be extracted by kinetic modeling which is necessarily subject to simplifying assumptions. These considerations and models will be briefly presented in the first part of the discussion section. A more rigorous analysis of reagent state dynamics is afforded by resorting to studies in the liquid phase, in which the atomic products are free to recombine between excitation pulses. This has been accomplished and reported for Br_2 and Cl_2 in liquid xenon[7] and more recently for ICl in liquid xenon.[6(b)]

Clearly, once the reaction of Eq. (1) is carried out to near completion, the product states—solid xenon doped with atomic halogens—can be investigated without interference from reagent states. The charge transfer states of such solids is our chief concern. Below we present a general motivation.

B. Charge transfer excitations in X:Xe

Electronic excitations in condensed rare gases have been the subject of extensive theoretical and experimental investigation. A rather complete account of this literature can be found in a recent monograph dedicated to this subject.[15] Among earlier reviews the treatment of excitons in rare gas crystals by Fugol is particularly informative.[16] It has been well established that the description of excitons in these wide gap dielectrics is intermediate between the Frenkel[17] and Wannier[18] descriptions. In the case of pure RGS, in the lowest excited state, the electron–hole binding is tight such that the states can be directly related to those of the isolated atoms. Hence, these states fit in the Frenkel description of excitons—an electron–hole pair on a single lattice site. In the case of higher excited states, large radius electron–hole pairs can be sustained. A hydrogenic Rydberg series that terminates in the conduction band is observed. The description of these states is then more appropriate in the framework of the Wannier exciton—an electron–hole pair separated by several lattice sites. The same also holds for the excited states of guest atoms or molecules that possess Rydberg states within the band gap of the RGS—xenon doped solid neon,[19] or NO doped RGS[20] are examples. The first excited states can be directly related to the isolated atomic or molecular states (although somewhat blue shifted), while the higher excited states do not bear any direct parentage to the isolated species and are well described as Wannier type excitons—electron–ion pairs trapped at the guest site.

A somewhat different situation is presented in the case of RGS doped with guest atoms of large electron affinity such as the halogens. We can however consider the charge transfer states of such a system in direct analogy to excitons bound to impurity sites in RGS. Consider an electron transfer from solid xenon to a guest atomic halogen. Due to the large electron affinity of the halogen atom, this will result in a deeply bound, hence well localized, electron on the guest site (see Appendix A) and will leave behind a hole in the valence band of the solid. The Frenkel limit of the negative ion–hole pair can be regarded as the localized, minimally two-center charge transfer exciton: namely the diatomic Xe^+X^- exciplex isolated in xenon. In the other extreme, given sufficient hole mobility, we may expect positronium-like Wannier excitons to represent the excited states of such a pair. It will be argued that the optically accessed states of the system are intermediate between these two limits—being between an *isolated molecular exciplex* and a *trapped charge transfer exciton* with a fully delocalized hole.

The molecular limit of these CT states, specifically those of a xenon crystal doped with atomic chlorine, has been considered theoretically by Last *et al.*[21–24] The semiempirical formalism of diatomics in ionic systems (DIIS) was developed for this purpose.[22] In this model, the Cl atom and its nearest neighbor xenons are considered explicitly (12 in the substitutional and 6 in the interstitial trap sites, respectively). The charge transfer states of the cluster, $Xe_{12}^+Cl^-$ (or $Xe_6^+Cl^-$), are then calculated as linear combinations of the valence atomic orbitals, and the effect of the extended solid is taken as a perturbation—a dielectric continuum that solvates the dipole of the cluster.[23] The Franck–Condon accessed charge transfer states of the complex are delocalized while the minimum energy configuration of the system closely resembles the gas phase triatomic $Xe_2^+Cl^-$ geometry. These results were shown to be in good qualitative agreement with our experiments.[23]

It is however now clear that ion–hole pairs separated by several lattice sites can be created optically in these solids.

This conclusion is based on the excitation spectra that will be discussed in this paper, and on the observation of charge separation and self-trapping that will be discussed in the following paper. It is then evident that the valence band of the solid need be considered more explicitly in order to account for delocalization of the hole on xenon atoms removed from the immediate vicinity of the negative ion. Thus we consider the valence hole states of the solid perturbed by the presence of the negative ion.

In the case of a perfectly crystalline solid xenon, the valence hole states are described by the tight binding, Bloch functions[25]:

$$\Phi_{\mathbf{k}}(\mathbf{r}-\mathbf{r}_j) = \sum_i e^{i\mathbf{k}\cdot\mathbf{r}_j} U_i(\mathbf{r}-\mathbf{r}_j) \tag{2}$$

in which U_i represents the atomic p_x, p_y, and p_z orbitals and the index j represents a particular lattice site. In the presence of the negative impurity ions and also the structural disorder of the solids of concern (the matrices studied in the present work are amorphous), the periodicity of the lattice is destroyed and k ceases to be a good quantum number. Thus the holes localize and are more appropriately represented by the Wannier functions constructed from the Bloch states:

$$\Psi_W(\mathbf{r}-\mathbf{r}_j) = \int_{\mathbf{k}_L}^{\mathbf{k}_0} e^{-i\mathbf{k}\cdot\mathbf{r}} \Phi(\mathbf{r}-\mathbf{r}_j)\, d\mathbf{k} \tag{3}$$

$$= \frac{N}{(\mathbf{r}-\mathbf{r}_j)} \sin\left(\frac{\Delta k(\mathbf{r}-\mathbf{r}_j)}{2}\right) e^{-i(k_0-\Delta k/2)} \times \sum_i U_i(\mathbf{r}-\mathbf{r}_j) \tag{4}$$

in which $\Delta k = |\mathbf{k}_L - \mathbf{k}_0|$, $|\mathbf{k}_0|$ is the norm of the wave vector at the zone boundary (π/a), while $\mathbf{k}_L$ is determined by the length of periodicity in the solid. In the case of disorder on the atomic scale, $|\mathbf{k}_L| \to 0$, and the Ψ_W become the atomic orbitals centered on individual xenon atoms. For $0 < |\mathbf{k}_L| < \pi/a$, the wave functions are centered on the atomic sites, however they have larger spatial extent than the atomic functions U_i. In order to optically induce an electron transfer from site j to a halogen atom at site i, the overlap of the electron wave function (localized on the halogen atom) and the Wannier function of the hole must be nonvanishing. In the case of highly disordered solids ($\mathbf{k}_L \to 0$), only transitions from neighboring xenon atoms should be possible, while in the case of solids with local order around the impurity site long range charge transfer is to be expected. The extent of the delocalization of the hole function should then be discernable from the range of the charge transfer transition. Finally, neither the hole nor the ion can be regarded as bare; they should both be dressed by electronic polarization waves. This is the case for the optically created pairs, since polarization relaxation in a solid of 1 eV valence bandwidth proceeds on the time scale of electronic absorptions. Thus, it is more appropriate to regard the charge transfer excitations as the creation of a pair of oppositely charged polarons. This is the static limit of excitons, appropriate for insulators as discussed by Fowler.[26] The picture then to bear in mind is one of an electron with infinite effective mass centered on the halogen atom and a hole centered on host lattice sites with limited mobility, however with large spatial extent.

This picture will be used for the simulation of excitation spectra in the reflection approximation to be presented in the discussion section. This will be done by making further simplifying approximations: the hole wave function will be represented by a delta function centered on the xenon atoms, and its spatial extent (overlap with the electron on the halogen atom) will be implicitly incorporated in the distance dependence of the transition matrix element, finally an attraction of Coulombic form will be assumed between the electron and hole.

II. EXPERIMENTAL

The experimental setup described in detail in I was used with minor modifications. Samples of rare gases doped with halogens or hydrogen halides were prepared in an all glass manifold and stored in glass bulbs.

Careful passivation of all gas handling surfaces was essential when switching between the various samples. The dopant gases were subjected to freeze–pump–thaw cycles to outgas the more volatile impurities, and finally distilled at low vapor pressure into the storage bulbs. HI (Matheson, 98% min.) was outgassed from a liquid nitrogen/*n*-propanol slush at 146 K, and then distilled at 273 K. Solid iodine (Fisher, resublimed) was outgassed at 273 K and sublimed at 298 K. HBr (Matheson, 99.8%) was outgassed at 77 K and then twice distilled from a liquid nitrogen/methanol slush at 175 K. Br_2 (Mallinckrodt, purified) was outgassed from a liquid nitrogen/*n*-butanol slush at 184 K and then distilled at 273 K. Fluorine (Matheson, 98% min.) was distilled at 77 K. Xenon (Spectra Gases, 99.9995%) was used without further purification.

The gas samples were transferred to a vacuum system attached to a closed cycle cryostat and subsequently pulse deposited onto a thin sapphire window cooled to 12 K. The resulting amorphous or polycrystalline solids were irradiated by an excimer-pumped dye laser system (Lamda Physik, EMG201/FL2002). In many experiments, the 308 nm output of the excimer laser was used directly, otherwise UV dyes in the 320–380 nm range were used or the output from visible dyes was frequency doubled to the 275–325 nm range. Weak-field excitation spectra of previously irradiated samples were obtained in the 220–400 nm region by using a Xe arc lamp and 0.3 m excitation monochromator. A new diffraction grating (1200 g/mm, 150 nm blaze) allowed for increased UV throughout and better resolution (typically better than 2 nm FWHM) in the excitation beam compared to the system used in I. Fluorescence from the samples was dispersed by a 0.25 m monochromator and detected by a photomultiplier tube of flat spectral response in the 200–800 nm range (Hamamatsu R666 and R758). In addition to the detection, signal averaging, and digitization electronics described in I, a Tektronix 2430 digital oscilloscope was used for data acquisition.

III. RESULTS

Emission spectra of Xe_2F, Xe_2Cl, Xe_2Br, and Xe_2I, in solid xenon at 12 K, are collected in Fig. 1. The Xe_2F spectrum is from a solid originally doped with molecular fluorine

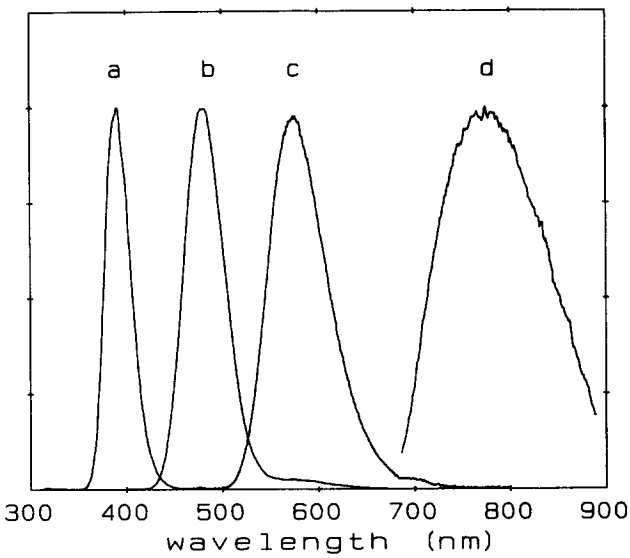

FIG. 1. Time integrated emission spectra of the triatomic $Xe_2^+X^-$ exciplexes in solid xenon at 12 K. (a) X = I; (b) X = Br; (c) X = Cl; (d) X = F. See the text for original sample compositions and excitation wavelengths.

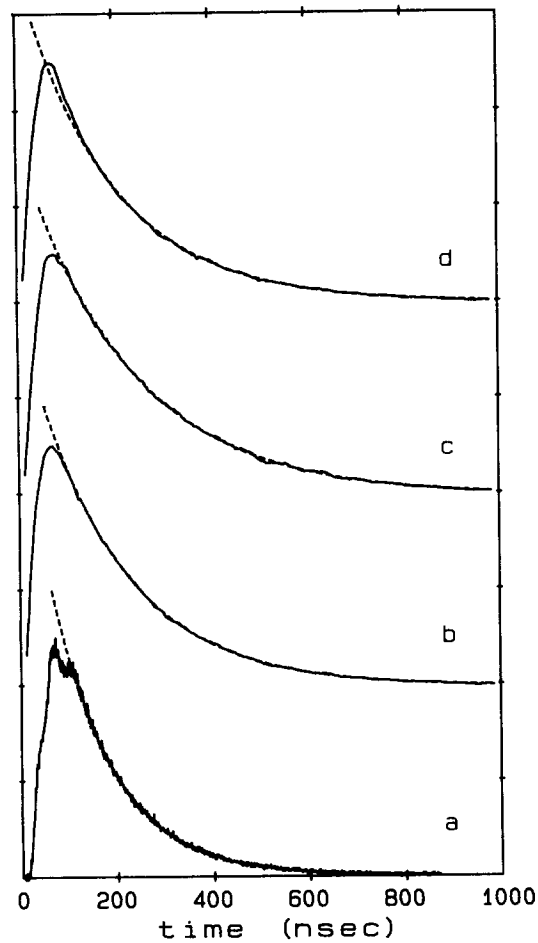

FIG. 2. Time evolution of the triatomic $Xe_2^+X^-$ exciplex emissions in solid xenon at 12 K and best fit single exponentials. (a) X = I, τ_{rad} = 130 ns; (b) X = Br, τ_{rad} = 185 ns; (c) X = Cl, τ_{rad} = 225 ns; (d) X = F, τ_{rad} = 190 ns. Excitation wavelength = 308 nm.

($M/R = 500$) and recorded after extensive irradiation at 308 nm. Xe_2Cl can be efficiently photogenerated in HCl or Cl_2 doped solid xenon by irradiation at wavelengths ranging from 360 to 280 nm; the details can be found in I. Xe_2Br spectra have been obtained from both HBr and Br_2 doped solid xenon. The example in Fig. 1 is from an HBr:Xe sample ($M/R = 500$), recorded after irradiation at 308 nm. The Xe_2I spectrum is from a sample originally doped with HI ($M/R = 500$) and after irradiation at 280 nm. The same spectrum, although requiring higher excitation fluence, could also be obtained by irradiation at 308 nm.

In all cases the triatomic exciplexes relax radiatively. This is verified by the temperature and concentration independence of observed fluorescence decay times. As in the case of Xe_2Cl, which was studied in detail over the temperature range of 12–160 K, it was verified that the fluorescence lifetimes at 12 K were within 10% the same as those measured in high temperature solids (140–160 K) prepared by freezing X_2:Xe solutions.[27] The exponential decays of Xe_2X emissions are shown in Fig. 2, along with the best fit exponentials. The measured lifetimes, at 12 K in solid xenon are: 190, 225, 185, and 130 ns for Xe_2F, Xe_2Cl, Xe_2Br, and Xe_2I, respectively. The observed spectroscopic parameters of the triatomic exciplexes in solid xenon are collected in Table I. The gas phase values are also reported in the table for the sake of comparison.

In these low temperature solids, the halogen molecules are permanently dissociated. With the exception of F doped matrices, the irradiated solids can be annealed with limited recombination of the trapped atoms. In the case of F doped solids, significant loss of Xe_2F emission intensity is observed upon warmup. This loss is attributed to the formation of the stable covalent xenon fluorides.

The charge transfer excitation spectra of the annealed atomic solids was recorded by monitoring the triatomic exciplex emissions. The effects of annealing and the temperature dependence of excitation spectra are similar in Cl, Br, and I doped solids. Representative spectra are shown from a Cl:Xe solid in Fig. 3. Preannealed spectra, Fig. 3(a), show a single

TABLE I. $Xe_2^+X^-$ emissions in gas and solid phases.

	F	Cl	Br	I
Gas phase				
Peak (nm)[a]	610	490	440	375
(eV)	2.03	2.53	2.82	3.31
τ_{rad} (ns)	152[a]	245[b]	245[a]	1000[c]
Solid phase				
Peak (nm)	775	573	480	390
(eV)	1.60	2.16	2.58	3.18
FWHM (cm^{-1})	2300	2100	2100	2000
(eV)	0.29	0.26	0.26	0.25
τ_{rad} (ns)	190	225	185	130
ΔE_{gs} (eV)	−0.43	−0.37	−0.24	−0.13

[a] Reference 28.
[b] Reference 29.
[c] Reference 30.

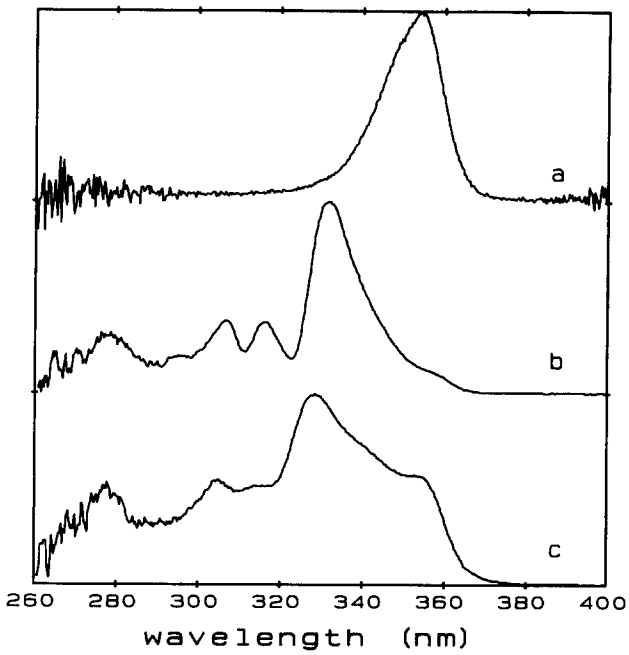

FIG. 3. Excitation spectra of Cl atom doped xenon solid recorded by monitoring 570 nm emission induced by monochromatized Xe arc lamp illumination. Original sample composition HCl:Xe 1:100. (a) Unannealed sample, recorded immediately following extensive irradiation at 308 nm; (b) annealed sample at 12 K, recorded after several temperature (12→50→12 K), and irradiation (308 nm) cycles. (c) Annealed sample at 50 K. The changes between 12 and 50 K in spectra (b) and (c) are reversible.

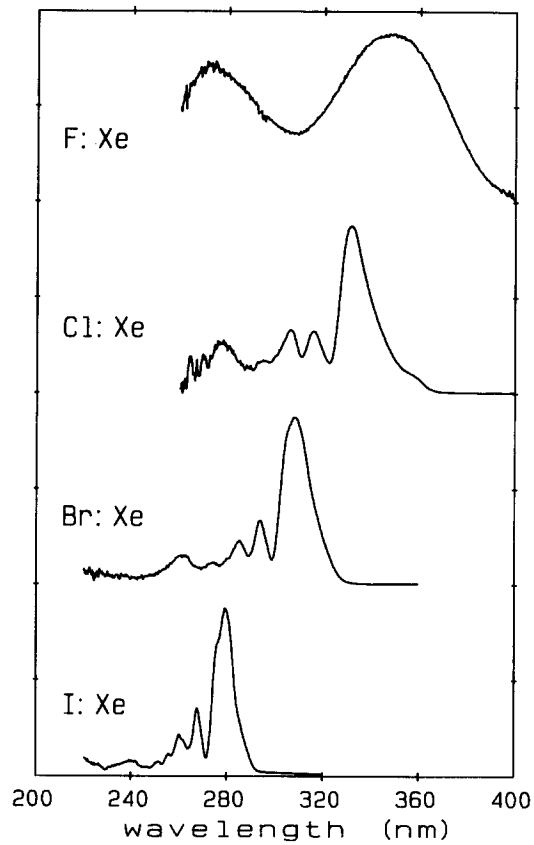

FIG. 4. Excitation spectra of X atom doped xenon solids recorded by monitoring $Xe_2^+X^-$ emissions at 12 K. The F:Xe spectrum is from an unannealed sample; all other spectra are from annealed solids.

TABLE II. X:Xe excitation spectra.

	F	Cl	Br	I
XeX ($X \leftarrow B$)				
Peak (nm)[a]	351	308	282	253
(eV)	3.53	4.03	4.40	4.90
Solid phase (13 K)				
Threshold (nm)[b]	391	358	325	290
(eV)	3.17	3.46	3.81	4.28
ΔE_{gs} (eV)	−0.36	−0.57	−0.59	−0.62
First peak (nm)	352	332	308	279
(eV)	3.52	3.74	4.02	4.44
Second peak (eV)	4.51	3.92	4.22	4.63
Third peak (eV)	···	4.05	4.35	4.77
Fourth peak (eV)	···	(4.15)[c]	(4.42)[c]	4.85
Fifth peak (eV)	···	(4.23)[c]	4.53	4.95
F.H. peak (eV)[d]	···	4.46	4.75	5.17
Solid phase (50 K)				
First peak (nm)		329	307	278
(eV)		3.77	4.04	4.46
Second peak (eV)		···	4.24	4.66
Third peak (eV)		4.07	4.37	4.79

[a] Reference 28.
[b] The thresholds for excitation are measured at 10% of the main peak height.
[c] Ill defined peaks (see spectra in Fig. 10).
[d] Peak assigned to free hole state.

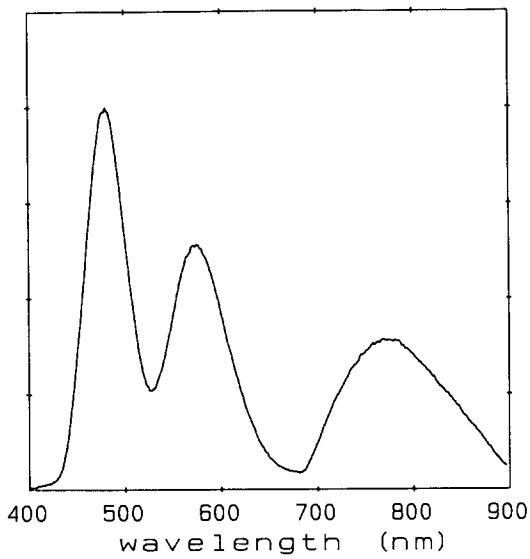

FIG. 5. Emission spectrum from 12 K xenon solid doped with F, Cl, and Br atoms; excitation wavelength = 308 nm. Excitation at 350 nm results in $Xe_2^+ Cl^-$ and $Xe_2^+ F^-$ emissions only (see the text).

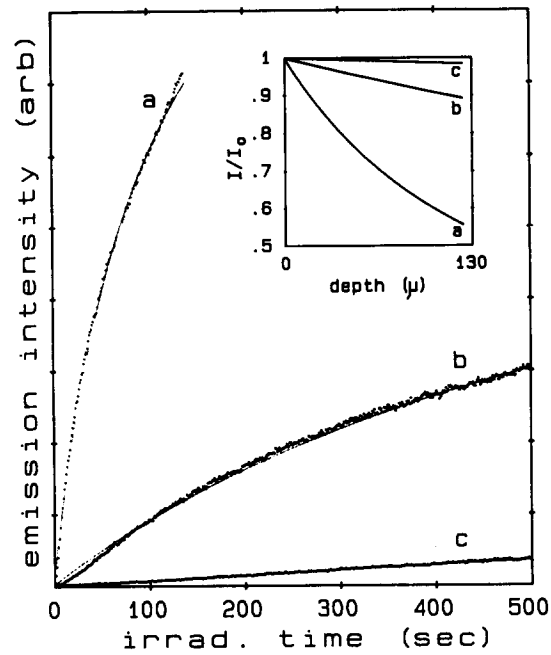

FIG. 6. Growth of $Xe_2^+ Cl^-$ emission in a Cl_2:Xe 1:1000 solid at 12 K irradiated at 308 nm for three different power levels: (a) 10.1 mJ/cm^2 at 5 Hz, (b) 3.5 mJ/cm^2 at 5 Hz, (c) 1.25 mJ/cm^2 at 5 Hz. The solid lines through the data points are calculated from the kinetic model shown in Eq. (7), for $\alpha = 1.5\times10^{-43}$cm^4 s, and $\beta = 7\times10^{-18}$cm^2. The inset shows the attenuation of the excitation field as a function of distance into the matrix slab.

maximum with a spectral shift from the gas phase diatomic XeCl ($B\rightarrow X$) emission that can be accounted for by a simple bulk dielectric model (see I). After several warmup and irradiation cycles (up to 50 K) structured excitation spectra are observed, Fig. 3(b). Dramatic, reversible temperature dependent changes in linewidths are observed as illustrated in Figs. 3(b) and 3(c). Excitation spectra from F atom and annealed Cl, Br, and I doped xenon matrices at 12 K are collected in Fig. 4. With the exception of F:Xe, the structure observed in the excitation spectra of all other halogens are nearly identical, such that they can be superimposed by a shift of the energy axis. In each case, immediately following the first main peak a sequence of four secondary peaks can be clearly identified. In all cases, at $\sim$0.7 eV to the blue of the main excitation band a weak broad absorption can be seen. Upon warmup, this structure broadens and most of the peaks coalesce. The observed peak centers are collected in Table II. In all cases while a well defined absorption threshold can be observed, high energy cutoffs cannot be identified. The blue edge of the reported spectra are strictly instrumental. Thus in a multiply doped solid, all halides can be simultaneously excited at short wavelengths. An example is shown in Fig. 5 from a solid doped with Br, Cl, and F. At 308 nm all three triatomics can be observed in emission. At 350 nm, in the same sample, only Xe_2Cl and Xe_2F emissions are observed. The radiative lifetimes measured in such multiply doped solids are within experimental error the same as those measured in individually doped solids, indicating the absence of any long range energy transfer between exciplexes despite their large transition dipoles.

The permanent dissociation of the molecular dopants and the photoproduction of the atomic halogens in these solids can be followed by monitoring the growth of the exciplex emission intensities as a function of irradiation time. Growth curves from a Cl_2 doped xenon solid are shown in Fig. 6 as a function of irradiation time and for three different irradiation intensities. Kinetic analysis of these growth curves is possible by taking into account both spatial and temporal evolution of the radiation field and reagents (see discussion in I). With simplifying assumptions these curves can be fit to kinetic models, and cross sections for both photoproduction and subsequent charge transfer excitations at a given wavelength can be extracted. The main simplifying assumptions pertain to bulk effects that cannot be well established. The most severe among these are the neglect of: scattering of the irradiation beam in these amorphous solids, diffusion of photoproducts out of the excitation volume, and local heating and annealing effects due to release of kinetic energy in both direct dissociation of the halogen molecules and the radiative dissociation of the exciplexes (annealing in turn is expected to alter photoproduction efficiencies). In view of these complications, perhaps the most reliable information obtained from the growth curves is the analysis of initial rates and their dependence on laser power. The reaction orders are obtained by fitting the initial parts of emission intensities to straight lines. The slopes of log–log plots of the linear growth rates vs laser power are used as reaction order.

IV. DISCUSSION

A. Spectroscopy of exciplexic states

The assignment of the 570 nm emission in Cl doped xenon matrices to the triatomic $Xe_2^+ Cl^-$ ($4\,^2\Gamma\rightarrow 1,2\,^2\Gamma$) has been firmly established previously. The picture of a localized molecular charge transfer complex for the emitter was established in I by spectral simulations using gas phase pair potentials. This assignment was more recently con-

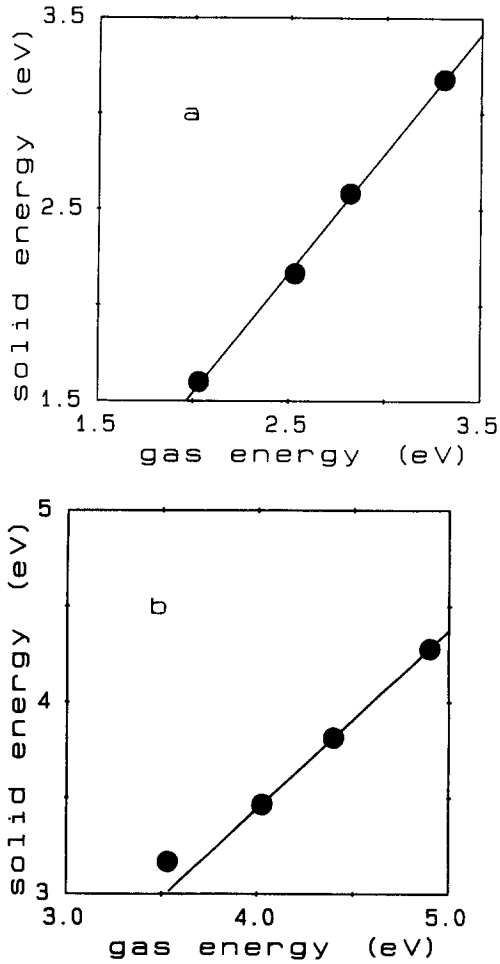

FIG. 7. Correlations between exciplex energies in gas phase and in solid Xe at 12 K. (a) Triatomic $Xe_2^+X^-$ emissions; see the text for discussion of Coulombic binding in these exciplexes, (b) gas phase XeX ($B \rightarrow X$) emission energies and thresholds for absorption in X doped solid Xe.

firmed by following the emission across phase transitions in gas, liquid, and solid xenon.[27] The emission band center undergoes a large red shift relative to the gas phase value due to the ionic-to-covalent nature of the transition. The large dipole of the upper ionic state is well solvated by the polarizable xenon host. The same observations and arguments hold for all of the $Xe_2^+X^-$ emissions. The direct correlation between emission maxima of the triatomic xenon halides in solid xenon and in the gas phase is shown in Fig. 7(a). The values of the band maxima and associated shifts relative to the known gas phase values $\Delta E_{gs} = E_{gas} - E_{solid}$, are collected in Table I. For a compendium of the gas phase spectra of rare gas halide exciplexes, see Ref. 28.

The values of ΔE_{gs} are not the same for the different halide exciplexes. In fact, the linear correlation in Fig. 7(a) indicates that the shifts can be written in terms of the gas phase emission energies as: $\Delta E_{gs} = aE_g + b$. The implication is that the shifts are proportional to the energies of the exciplexes. This dependence can be rationalized by considering a picture of Coulombic binding in the $Xe_2^+X^-$ exciplexes, and the simple cavity dielectric model for the spectral shifts. For strictly Coulombically bound exciplexes, the gas phase energies of $Xe_2^+X^-$ would be given as

$$E = \mathrm{IP(Xe)} - E_{\mathrm{bind}}(Xe_2^+) - \mathrm{EA(X)} - \frac{C}{R} \tag{5}$$

in which IP(Xe) is the ionization potential of Xe, E_{bind} (Xe_2^+) is the binding energy of Xe_2^+, EA(X) is the electron affinity of X, and R is the sum of ionic radii of the Xe_2^+ and X^- ions. The gas to solid energy shifts predicted by the cavity model are given by[31]

$$\Delta E_{gs} = \frac{-8(\epsilon - 1)\mu^2}{(2\epsilon + 1)d^3} \tag{6}$$

in which μ is the dipole of the exciplex, d is the diameter of the cavity, and ϵ is the dielectric constant of the Xe solid. If the same picture of Coulombic binding also holds in the solid phase, then we expect that both the dipole μ and the cavity diameter d will be proportional to R, yielding an approximate dependence of

$$\Delta E_{gs} \propto \frac{-1}{R}. \tag{7}$$

The observation of the same dependence of the exciplex energy and spectral shift on the halide ionic radius corroborates the picture of simple Coulombic binding of the solid phase exciplexes.

A fit to Eq. (7) using the literature ionic radii[32] of Cl^-, Br^-, and I^- and the observed values of ΔE_{gs} yields 1.64 Å as the ionic radius of Xe_2^+. This value is in good agreement with the geometry and bond lengths used to simulate the $Xe_2^+Cl^-$ emission spectrum in I. Deviation from Eq. (7) in the case of fluorine is attributed to the well known saturation effect in electron affinities of halogens—the small F^- ion cannot accommodate the full charge transferred from the xenons. This effect is thus expected to lower the value of the $Xe_2^+F^-$ dipole and so reduce ΔE_{gs}.

We can extend this simple picture to the analysis of the linewidths. The breadths of the emissions are due to the bound to repulsive nature of the exciplexic transitions. The interxenon equilibrium bond length is ~ 1 Å shorter in $Xe_2^+X^-$ than the Xe–Xe nearest neighbor distance of 4.34 Å. Thus the major contribution (~ 1300 cm^{-1}) to the linewidth is due to the Xe–Xe coordinate and is common to the entire family of Xe_2X exciplexes. Indeed the observed widths of all triatomic emissions are very similar, FWHM = 2300, 2100, 2100, 2000 cm^{-1} for Xe_2F, Xe_2Cl, Xe_2Br, and Xe_2I (the additional 800 to 1000 cm^{-1} contribution to the linewidths comes from the bound to repulsive nature of the Xe_2–X coordinate). As in the case of $Xe_2^+Cl^-$, we contend that the emission profiles can be adequately represented by the gas phase potentials.

The excitation thresholds (listed in Table II) can be well correlated with the known gas phase XeX ($B \rightarrow X$) emissions, with some deviation in the case of F doped solids. This is shown in Fig. 7(b). This supports the argument that the observed excitations derive their origins from the diatomic (B) states. However, it should become obvious in Sec. IV D below that, with the exception of XeF, the optically accessed charge transfer states are more aptly described as delocalized states as opposed to the diatomic Xe^+X^- (B) states. While approximate, it is convenient to treat the entire

charge transfer photocycle of halogen doped rare gas solids via the localized molecular potentials, namely:

$$Xe + X + h\nu \rightarrow Xe^+X^-(B)\,, \tag{8a}$$

$$Xe^+X^- + Xe \rightarrow Xe_2^+X^-(4\,^2\Gamma)\,, \tag{8b}$$

$$Xe_2^+X^- \rightarrow Xe + Xe + X + h\nu'\,. \tag{8c}$$

This is the basis of the four level laser model which we had previously presented along with gain measurements in both solid[5] and liquid xenon.[6(a)] We will use this terminology to discuss the kinetics of photogeneration of halogen atoms in these solids. Note that this photocycle represents a sensitive scheme for the detection of halogen atoms in xenon: the CT absorption in Eq. (8a) is intense, the interconversion in Eq. (8b) occurs with near unity probability, and the relaxation of the triatomic in Eq. (8c) is strictly radiative. This is the scheme on which we rely in determining the extent of atomization in the matrices.

B. Lifetimes and excitation transfer

While both emission and excitation spectra are well correlated with their gas phase counterparts (triatomic and diatomic exciplexes, respectively), the radiative lifetimes of the triatomics are not. The measured radiative lifetimes in solid xenon, together with the known values from the gas phase are collected in Table I. The absence of any correlation between these sets of values is disturbing and its reasons are not understood. The solid state lifetimes span a much narrower range, and the order $\tau_{Cl} > \tau_F \gtrsim \tau_{Br} > \tau_I$ correlates nicely with the electron affinities of the halogens. This is expected for these emissions since the transition dipoles are determined by the extent of charge transfer in the ionic upper state.

The absence of any long range energy transfer between exciplexes is expected based on the large Stokes shifts between emission and excitation spectra—a characteristic feature for all Xe_2X exciplexes. This argument holds not only for energy transfer between different xenon halides, as demonstrated by the multiple doping experiments in which the same lifetimes are observed as in the case of singly doped samples, but also for intermolecular transfer among exciplexes of a given halogen. The latter is verified by the absence of any concentration dependence in measured lifetimes for initial sample concentrations of $X_2(HX)$:Xe as high as 1:100. Thus despite the very large dipoles and transition dipoles of these ionic states, due to the absence of any appreciable overlap between excitation and emission bands, long range energy transfer mechanisms are absent (see, for example, the Förster–Dexter formulation for long range energy transfer[33]). The absence of excitation hopping guarantees that large exciplex densities can be created in a solid, without deactivation due to excitonic annihilation, or migration assisted deactivation at impurity sites.

C. Photogeneration of halogen atoms

There are in principle several possible mechanisms for the photoproduction of exciplexes in HX or X_2 doped solid xenon by irradiation with near UV photons. These are:

(i) Photodissociation followed by photoassociation:

$$X_2(HX) + h\nu \rightarrow X + X(H)\,, \tag{9a}$$

$$X + Xe + h\nu \rightarrow Xe^+X^-\,, \tag{9b}$$

$$Xe^+X^- + Xe \rightarrow Xe_2^+X^-\,. \tag{9c}$$

(ii) Two-photon excitation of the parent dopant, and its subsequent reactive quenching:

$$X_2(HX) + 2h\nu \rightarrow X_2^*(HX^*)\,, \tag{10a}$$

$$X_2^*(HX^*) + Xe \rightarrow Xe^+X^- + X(H)\,, \tag{10b}$$

$$Xe^+X + Xe \rightarrow Xe_2^+X^-\,. \tag{10c}$$

(iii) Two-photon harpooning:

$$X_2(HX) + Xe + 2h\nu \rightarrow Xe^+X_2^-(HX^-)\,, \tag{11a}$$

$$Xe^+X_2^-(HX^-) \rightarrow Xe^+X^- + X(H)\,, \tag{11b}$$

$$Xe^+X^- + Xe \rightarrow Xe_2^+X^-\,. \tag{11c}$$

In all cases, the reactive quenching of the diatomic exciplex to form the triatomic (9c), (10c), and (11c) is a step that can be assumed fast. This assumption is borne out by the absence of any diatomic emissions in our experimental spectra even though the radiation probability from diatomic states is almost two orders of magnitude larger than from triatomics.[28]

All of the triatomic exciplexes relax by radiative dissociation to form neutral halogen atoms. Since the interrogation volume is static, both reagents and products are illuminated by the radiation field. If the photolysis wavelength is below the threshold for inducing the photoassociation step (8b), then the four-level photocycle described above provides for a sensitive method of monitoring the growth of the X atom concentration. With the exception of iodine, this condition is satisfied for all halogens in xenon when irradiated at 308 nm. Therefore the observation of growth in emission intensity with irradiation time implies permanent dissociation. Examples of such growth curves, from a Cl_2–Xe solid, irradiated at 308 nm, and at three different fluences, are presented in Fig. 6. Since charge transfer absorptions possess oscillator strengths of near unity, in thick samples the halogen atoms will also hamper further photogeneration by absorbing the incident radiation. This effect should be explicitly included in any kinetic treatment of growth curves. Nevertheless, from initial rates of growth alone, the power dependence of dissociation can be estimated. In the case of the Cl_2 data of Fig. 6, the power dependence is 2.5. The growth rates in all studied cases are nonlinear.

Complications also arise due to the presence of imperfections in the matrices. Matrices formed by pulsed vapor deposition on a cold surface are not well defined solids. This consideration is particularly important in the case of xenon where optically nonscattering solids are nearly impossible to produce. Our data definitely refer to amorphous solids in which microcrystallites may exist, however, judging from the frosty appearance of these matrices it would be impossible to characterize them as crystalline. Thus, while dissociation may be inhibited in fcc cages, it may not be near vacancies or imperfections. Additional problems are caused by the accommodation by the matrix of the large excess kinetic energy released in both the photodissociation steps and the

radiative relaxation of the exciplexes. It is not clear whether this will result in local annealing of the matrix, or its amorphization. In any case, it can cause changes in the structure of the matrix over the course of an experiment. This is believed to be the source of induction periods observed in the growth curves for some of the systems to be discussed.

Due in part to the difficulties mentioned above, and to experimental problems in reproducing matrix characteristics and irradiation beam properties for the different samples and wavelength ranges probed, we will not attempt a detailed comparison and correlation of all the experimental results. Rather, we will divide the general discussion into two sections concerning the hydrogen halides and the molecular halogens.

1. HX:Xe

Growth curves from an HCl:Xe solid irradiated at 308 nm were presented in I. The rejection of mechanism (i) in this case is straightforward. HCl is efficiently atomized at photon energies (between 308 and 360 nm) much below its dissociation limit[34] of 4.43 eV. A minimally two-photon process is therefore required, and this is verified by the power dependence of 1.9 ± 0.2 obtained from the initial rates. Mechanism (iii) is favored in this case based on the absence of any dissociation in the gas phase at the same excitation wavelength range (for a detailed discussion see I).

In the case of HI and HBr doped matrices, the irradiation energy at 308 nm is above their respective dissociation limits. Therefore, even though weak, direct dissociative absorptions are possible at this wavelength.[34] The dissociative absorptions of HBr and HI properly begin near 250 and 280 nm, respectively. More importantly, both molecules have strong absorptions ($\sigma = 10^{-18}$ cm^2) in the region energetically accessible by two photons at 308 nm. The power dependence in the case of HBr could not be extracted from initial rates of growth due to a long induction period. For HI, at 280 nm a second order (2.0 ± 0.2) dependence is observed while at 308 nm a third order (2.8 ± 0.2) dependence is observed. This difference is well rationalized since 308 nm is below the excitation threshold of I:Xe while 280 nm corresponds to the excitation maximum (see spectrum in Fig. 4). That the change in photogeneration orders is due to the detection step was verified by testing the detection power dependence after extensive irradiation of the solid. At 308 nm the $Xe_2^+ I^-$ emission has a second order dependence on excitation power while it is first order at 280 nm. Thus, based on the nonlinearity of the photogeneration, we can exclude the direct photodissociation mechanism of Eq. (9) as a significant channel of permanent photodissociation for all HX at these wavelengths. However, the present data do not allow for a clear determination of whether mechanism (ii) or (iii) [Eqs. (10) and (11)] is the operative one.

2. X_2:Xe

For both F_2 and Br_2, the molecular dissociative absorptions are weak[34] at the irradiation wavelengths commonly used (e.g., 308 nm), σ_{F_2} (308 nm) $\leqslant 10^{-21}$ cm^2, σ_{Br_2} (308 nm) $\leqslant 10^{-20}$ cm^2. Yet experiments in solid Xe show strong exciplex emissions indicating the presence of F and Br atoms. Growth curves in F_2:Xe solids are characterized by a very fast initial rise to a plateau region followed by a slow decay. This decay is attributed to the formation of the stable covalent species XeF_2 which is transparent in the near UV. This hypothesis is verified by the fact that only in F doped solids does the exiplexic emission significantly diminish upon annealing. In the case of Br_2 doped solid xenon, the exciplexic emission at 480 nm grows in time in a manner similar to Cl_2 to be discussed in detail below.

Perhaps the most complicated system is that of Cl_2 doped solids. The molecular dissociative absorption is significant at 308 nm (1.9×10^{-19} cm^2) and therefore this transition will certainly be accessed even if it does not result in permanent dissociation. Yet a power dependence of 2.5 ± 0.1 is observed for the growth rates indicating the likelihood of mechanism (ii) or (iii) as the operative one. Since the power dependence studies are conducted by attenuating the irradiation laser, it is not possible to distinguish between fluence and intensity dependences which could in principle distinguish the coherence of the nonlinear excitation. The pertinent kinetic equations which represent both mechanisms (ii) and (iii) can be reduced to

$$\mathrm{Xe} + \mathrm{Xe} + \mathrm{X}_2 + 2h\nu \xrightarrow{\alpha} \mathrm{Xe}_2^+ \mathrm{X}^- + \mathrm{X}\,, \tag{12a}$$

$$\mathrm{Xe} + \mathrm{Xe} + \mathrm{X} + h\nu \xrightarrow{\beta} \mathrm{Xe}_2^+ \mathrm{X}^-\,, \tag{12b}$$

$$\mathrm{Xe}_2^+ \mathrm{X}^- \xrightarrow{1/\tau_r} h\nu' + \mathrm{Xe} + \mathrm{Xe} + \mathrm{X}\,. \tag{12c}$$

Since the studies are conducted in solid xenon, explicit account of the Xe stoichiometry is not essential in Eqs. (12a)–(12c), nevertheless they are included for clarity. In the absence of nonradiative decay channels for $Xe_2^+ X^-$, it follows that

$$\frac{d[h\nu']}{dt} \propto \frac{1}{\tau_r}[\mathrm{Xe}_2^+ \mathrm{X}^-]\,, \tag{13}$$

i.e., the emitted photon intensity is directly proportional to the exciplex number density. The exciplex number density can then be obtained as a function of irradiation time by explicit account of the depth profiles of all pertinent reagents, $h\nu$, X_2, X, and $Xe_2^+ X^-$. To this end, the experimentally determined thickness of the matrix ($130\,\mu$) is divided into 20 optically thin slabs and the rate equations integrated over both time and depth. The result of this simulation for $\alpha = 1.5 \times 10^{-43}$ cm^4 s and $\beta = 7 \times 10^{-18}$ cm^2 is shown superimposed on the experimental data in Fig. 6. We note that there are only two parameters in the model and they fit the curves with good agreement for three different powers. The simulated initial rates have the correct 2.5 order power dependence. This fractional order arises naturally from the explicit inclusion of the spatial dependence of the rate equations. The severity of the concentration gradients can be seen from the inset to Fig. 6 where the profile of the excitation photon density along the thickness of the slab is shown. At low powers or early times, when the X concentration is very

small, the irradiation beam traverses the slab with uniform intensity throughout. However, as soon as a significant X concentration is built up, the excitation beam will be severely attenuated due to the large charge transfer absorption cross sections in Eq. (8a). Since the photoproduction step (12a) is second order in photon density, the attenuation of the radiation field will strongly reduce the rate of this process. The X atom depth profile follows the laser intensity profile, while the X_2 profile has the opposite dependence on distance. In concentrated matrices, $M/R < 1000$, the ablation limit is reached prior to atomization of all starting material.

Despite the good agreement between model and experiment, several words of caution are in order. The model is an oversimplification, several aspects are ignored: (a) we ignore the possibility of single photon absorptions in X_2 which are present even though they may not yield any dissociation, (b) we ignore the scattering nature of the solid which, as in the consideration in (a), would also strongly attenuate the photon flux, (c) it is assumed that there is no atomic recombination, (d) all possible bulk effects such as photoannealing or destruction of the solid due to kinetic energy release in dissociation steps are ignored. These assumptions are made because there are no direct quantitative methods to account for these bulk effects. The only discrepancy between fit and data is the slight induction period at the intermediate power level. This cannot be reproduced by the model and is most likely due to changes in the bulk properties of the sample.

In view of all of the model assumptions the reliabilities of the cross sections obtained are to be questioned. The charge transfer absorption cross section β can be estimated independently. If we assume a unity oscillator strength for this transition, and a radiative lifetime of 5 ns for the XeCl (B) state, then from the excitation line shape an absorption cross section of 10^{-18} cm^2 can be deduced. The agreement between this value and that determined from the model should be regarded as excellent in view of the assumptions. The two-photon cross section α of Eq. (11a) is subject to greater error. However, if we note that all of the major assumptions made correspond to either overestimating the photon density or to overestimating the permanent dissociation probability of the X_2, it becomes obvious that α is a lower bound value for the case of solids. More recently, α was measured directly by power dependent transmission measurements in Cl_2/Xe liquid solutions, a value of $\alpha = 6\times10^{-45}$ cm^4 s was obtained there.[7] The agreement between these values is acceptable in view of the model assumptions in the solid state measurements, and also the expectation of a reduction in α in the liquid phase due to lower densities (measured at 200 K).

While the kinetic analysis does not distinguish between mechanisms (ii) and (iii), the direct dissociation mechanism, mechanism (i), can clearly be rejected for all X_2. It is also possible to reject mechanism (ii) as a significant channel of permanent photodissociation. This conclusion is reached based on studies of Cl_2 in pure Ar and Kr hosts. In accord with previous studies,[8] when such matrices are irradiated at 308 nm, only the recombinant $A\rightarrow X$ emission is observed. No significant diminution of this molecular emission is observed over extended periods of irradiation (>3 h at 10 Hz) at power levels much higher (>10 mJ/cm^2) than those used in solids containing xenon. Some permanent dissociation does however occur under these conditions. This is verified by the observation of $A\rightarrow X$ emission upon warm-up of the irradiated solids. This thermoluminescence, due to geminate recombination, is however very weak and implies a degree of dissociation that can easily be attributed to events near imperfections in the solid. In contrast with these results, in either Cl_2:Xe solids or Ar and Kr hosts doubly doped with Cl_2 and Xe, the exciplexic emissions grow and the molecular emissions decay with irradiation time. The experiments in pure Ar and Kr hosts serve two purposes: first they establish that the presence of xenon is essential for the permanent two-photon dissociation of Cl_2—hence the rejection of mechanism (ii); second, they establish that our experiments are in accord with the previous studies of the rigid cage effect and that the facile atomization of the halogens in xenon containing solids is not due to special experimental effects, such as the preparation of samples.

The microscopic implications of this conclusion are of great significance. In the direct dissociation mechanism, at 308 nm, the excess energy available to the Cl atoms is $[E(h\nu) - D_0^\circ(Cl_2)]/2 \sim 0.75$ eV. In the two-photon harpoon mechanism, the excess energy available to the ejected atom can be calculated as $[2E(h\nu) - E(Xe^+Cl^-) - D_0^\circ(Cl_2)]/2 \sim 1$ eV. Efficient two-photon production of Cl from Cl_2 is observed at wavelengths as long as 360 nm. Thus it is clear that the recoil energy itself is not the determining factor in the permanent dissociation and cage exit of the halogen. A more plausible explanation is obtained by consideration of the potentials involved in these processes. In the case of direct dissociation via the repulsive $^1\Pi$, $^3\Pi$ potentials of the molecular halogen, if the dissociation products linger in the matrix cage due to direct hits with cage atoms, then with sufficient loss of energy (which typically occurs on a subpicosecond time scale, see Ref. 13) the Cl atoms can cross over to one of the attractive bound states. In the case of the ionic dissociation channel, once the electron harpoons from xenon to Cl_2, the Xe^+X^- coordinate becomes attractive while the X^-–X coordinate becomes repulsive (the vertical transition from Cl_2 to Cl_2^- leads to the repulsive wall of the molecular ion[14]). Additionally, the cage atoms, which are more polarizable than Cl, are attracted by the dipole of the ionic exciplex. This situation will persist for the duration of the exciplex lifetime ($\sim10^{-7}$ s) during which time there is ample opportunity for cage rearrangements. A partial cage collapse to cluster around the dipole will also help eject the neutral Cl atom. Direct evidence for clustering of solvent atoms around the exciplex has been obtained in the liquid phase studies.[6(b)] Thus while a strong cage effect is observed in direct dissociation via covalent potentials, in the case of dissociation via ionic potentials, a propensity for the cage to eject the neutral dissociation product and to cluster about the ionic product is to be expected. The active participation of the solvent atoms in ejecting the trapped atom can be thought of as a "negative cage effect." Its reality is at present being tested by trajectory calculations. Experiments in better characterized solids are essential to verify this hypothesis.

TABLE III. XeX (X) state potentials and XeRg pair potentials; minimum separations (r_m) and well depths (ϵ).

X	r_m (Å)	ϵ (eV)	Ref.
F	2.293	0.146	35
Cl	3.32	0.0347	36
Br	3.80	0.0280	37
I	4.30	0.0299	37
Ne	3.8	0.0064	38
Ar	4.01	0.0164	36
Kr	4.12	0.0202	37
Xe	4.36	0.0242	38

TABLE IV. XeF (X, B, D) state parameters (from Ref. 39) and resulting harmonic oscillator and Morse potential parameters. Values in parentheses in (eV), and $\mu_{XeF} = 15.597$ amu.

	X	B	D
T_e (cm^{-1})	0	28 811	38 051
		(3.752)	(4.718)
ω_e (cm^{-1})	225.4	309.0	350.1
	(0.0279)	(0.0383)	(0.0434)
$\omega_e\chi_e$ (cm^{-1})	10.9	1.50	1.90
D_e (cm^{-1})	1175	42 783	44 080
	(0.146)	(5.304)	(5.465)
R_e (Å)	2.293	2.631	2.513
k_e (eV Å^{-2})	3.13	...	...
α^2 (Å^{-2})	116.2	...	...
β (Å^{-1})	...	0.7412	0.8906

D. X:Xe excitation spectra

A cursory examination of the excitation spectra in Fig. 4 reveals a strong similarity in the structure of the Cl:Xe, Br:Xe, and I:Xe absorptions; in fact, the structure in these spectra can be matched by a simple shift in the energy abscissa (see Fig. 10). While the peak widths decrease somewhat, and have a smaller temperature dependence in the series Cl, Br, I; the overall similarity of the spectra suggests that the observed structure is characteristic of the extended solid and not sensitive to the particulars of the dopant. There is a marked difference between these spectra and the F:Xe spectrum. The peaks in the F:Xe spectrum are much broader and do not display the same characteristic pattern as the other halogens.

The key to understanding the difference between xenon doped with F vs the heavier halogens can be found in the ground state structure of these atomic solids. In as much as the optical CT transitions are governed by Franck–Condon rules, inspection of the ground state potential surfaces of these systems is essential for the interpretation of the spectra. The known gas phase pair potentials are the natural starting point for such a consideration. The minima and depths of Xe–X and Xe–Rg pair potentials are collected in Table III. A comparison of these parameters clearly reveals that with the exception of F, the Xe–X potentials are dominated by dispersion forces. The Xe–I pair potential is nearly identical with that of Xe–Xe. In the series I, Br, Cl, the interaction becomes successively more"chemical" in nature, with increasingly greater ionic admixture in the ground state character, such that the Xe–Cl potential is nearly twice as deep as that of Xe–Ar and its minimum, 3.23 Å, is substantially shorter than the sum of van der Waals radii of 4 Å. However, the situation is drastically different in the case of Xe–F. The depth of the potential in this case is more than an order of magnitude larger than that of Xe–Ne, and in fact the XeF(X) state minimum separation is 0.34 Å shorter than that of the deeply bound ionic XeF(B) state (see Table IV). Quite clearly there is extensive charge transfer—"chemical character"—in the ground state potential of XeF. It then becomes clear that the ground state surfaces of solid xenon doped with the heavier halogens should be well represented by pairwise additive potentials:

$$V_{gnd}(\mathbf{r}) = \sum_i V_{Xe\text{-}X}(\mathbf{r} - \mathbf{r}_i) \qquad (14)$$

in which i labels the xenon atoms, and X = I, Br, Cl, with the gas phase pair potentials as a useful starting point for $V_{Xe\text{-}X}$. Moreover, it should be clear that this description is inappropriate for the case of F doped solids, and that the latter is better described as XeF isolated in solid xenon. In what follows we will treat the excitation spectra of fluorine doped solids as that of the diatomic xenon fluoride perturbed by the matrix, while in the case of the heavier halogens we make no such assumption.

1. XeF absorption spectrum

The gas phase potentials for the covalent ground state, and the ionic excited states of the diatomic xenon fluoride are well characterized both by experiment[39] and theory.[40] Two intense charge transfer absorptions are to be expected from XeF(X): $B \leftarrow X$ and $D \leftarrow X$. Both B and D state potentials can be well represented by the Morse form:

$$V_{Morse}(r) = T_e + D_e(e^{-2\beta(r-r_e)} - 2e^{-\beta(r-r_e)}), \qquad (15)$$

the potential parameters of which are collected in Table IV. Using the gas phase potentials for all three states (shown in Fig. 8), we explicitly simulate the expected absorption spectra. The transition probability is given as

$$P(\omega) = \frac{8\pi^3}{3h^2c}|\mu_{eq}|^2 \sum_f |\langle\psi_f|\psi_i\rangle|^2 \delta(\hbar\omega - \hbar\omega_f - T_e) \qquad (16)$$

in which μ_{eq} is the transition dipole integrated over electronic coordinates; ψ_i and ψ_f are vibrational wave functions in the ground and excited states, respectively, and T_e is the electronic origin of the ionic state. For ψ_i we shall use a simple harmonic wave function:

$$\psi_i(r) = \left(\frac{\alpha^2}{\pi}\right)^{1/4} \exp\left(\frac{-\alpha^2}{2}(r - r_e)^2\right) \qquad (17)$$

for parameters, see Table IV. The excited state wave functions ψ_f are calculated by the numerical method due to Cooley.[41] The Franck–Condon factors are then evaluated and the summation in Eq. (16) is carried out for 40 excited states in each of the B and D manifolds. The resultant stick spectra are shown in Fig. 9. The only adjustment made in this calculation was that of T_e. A reduction of T_e by 0.42 eV for both B

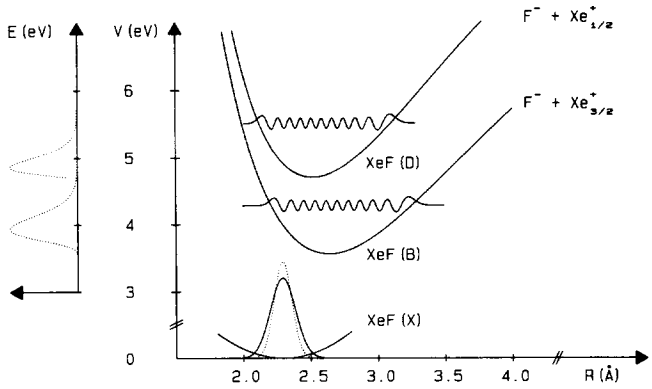

FIG. 8. XeF potentials and wave functions used to simulate the diatomic ($B \leftarrow X$) and ($D \leftarrow X$) absorptions. The dotted spectra on the left of the figure are calculated by reflecting the XeF (X) $v = 0$ probability distribution (solid Gaussian) at the upper states' repulsive walls. The XeF(X) $v = 0$ wave function (dotted Gaussian) and the $v = 20$ wave functions for the upper states are used in the calculation of Franck–Condon factors for the transitions (see Fig. 9). The potential parameters are listed in Table IV.

and D states, i.e., a red shift of the electronic origins, results in a good match between the maxima of the simulated Franck–Condon envelopes and the experimental excitation spectrum (shown as solid curve in Fig. 9). This adjustment accounts for the static dielectric shift which was discussed in Sec. IV A, and is in line with the predictions of the simple cavity cell model.

The general agreement between model and experiment lends credence to the assumption that indeed the charge transfer states of the diatomic xenon fluoride are being monitored, and hence to the assignment of the two broad bands to XeF($B \leftarrow X$) and XeF($D \leftarrow X$). The separation between these two transitions, both in the gas and solid state, is essentially the spin–orbit splitting in Xe^+. There are two obvious discrepancies between model and experiment: the experimental spectrum is vibrationally unresolved; and the observed bands are substantially broader than those of the simulation, e.g., in the case of the $B \leftarrow X$ transition the experimental width (FWHM) is 0.55 eV, while the simulation yields 0.44 eV. The absence of vibrational structure is not due to the lack of experimental resolution—the lines are broad and completely coalesced. The obvious major contributer to this broadening is that of dynamical dielectric shift (dielectric relaxation). Polarization relaxation in this system can be estimated from the valence bandwidth of solid xenon to occur on the time scale of absorption. Moreover, it is to be expected from the observed 0.42 eV static shift that the same mechanism (dipole–induced dipole interactions) provides an efficient channel for coupling the molecular exciplexic vibrations to the lattice phonons. In the absence of any vibrational resolution it is not possible to infer the extent of this coupling from the experimental data. It is also dangerous to ascribe the discrepancy between experimental and simulated overall bandwidths to dielectric relaxation alone. There are several factors that potentially contribute to this mismatch. The most serious experimental effect is that of inhomogeneous broadening—these solids could not be well annealed due to the reactivity of F with xenon, with presumed formation of XeF_2, at elevated temperatures. In the case of the simulations, the assumption of gas phase potentials is to be questioned; a softer ground state potential or a steeper repulsive wall in the excited state, would result in a broader absorption profile. While these modifications could easily be incorporated in the model to produce a match with experiment, they could not be well justified. In their studies on XeF trapped in Ar and Ne matrices, Brus and co-workers have demonstrated that in fact the opposite is true—the XeF ground vibrational frequency is $\sim 10\%$ higher in Ar than in the gas phase.[42] While we refrain from quantifying the line-broadening effects we conclude that the molecular states, in particular the vibrations of the exciplexic states, are strongly perturbed by the matrix.

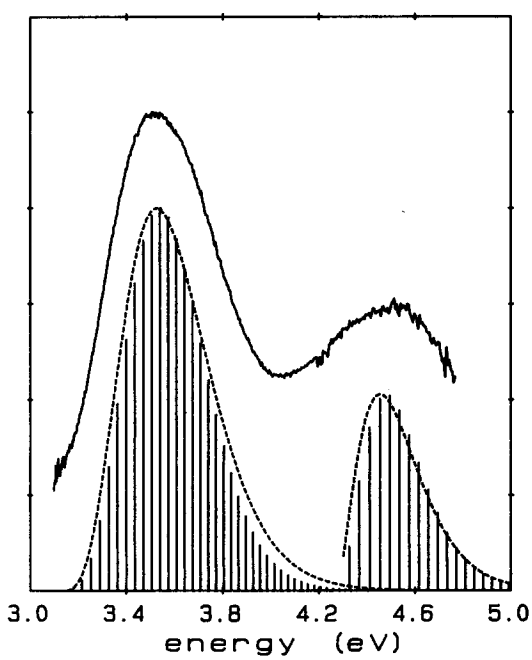

FIG. 9. XeF absorption spectra. Upper trace is observed F:Xe absorption at 12 K. The dashed curves are the results of the XeF ($B \leftarrow X$) and XeF ($D \leftarrow X$) reflection approximation simulations. The vertical sticks are the Franck–Condon factors for the ($B \leftarrow X$) and ($D \leftarrow X$) transitions. The simulated spectra are shifted by -0.42 eV to account for solvation of the exciplexes' dipoles, and normalized to match the observed intensities.

Given the evidence that the exciplexic vibrational states are strongly perturbed by the medium, and also the fact that the ground state nuclear wave function is mostly limited to spanning the repulsive wall of the ionic potentials (see Fig. 8), it should be possible to reproduce the absorption profiles of these localized CT transitions with the computationally more simple method of the reflection approximation.[43] This approximation is designed for the treatment of diffuse bound–free spectra in the gas phase; the similarity of the experimental spectra to such transitions suggests the applicability of the method in the present case. The presentation of this alternate approach here is to demonstrate its validity, since the analysis of the spectra of the heavier halogens will be based on a formulation akin to this approximation.

In the case of a bound–free transition, or equivalently a transition to a state in which the vibrational wave functions

are strongly damped, the overlap integral between nuclear eigenfunctions is evaluated by assuming for the free state delta functions at the classical turning points of the potential. The absorption intensity profile in this limit, the equivalent of Eq. (16), is given by

$$P(\omega)=\frac{8\pi^3}{3h^2c}|\mu_{\rm eq}|^2\int dr|\psi_i(r)|^2\delta[\hbar\omega-V_f(r)] \quad (18)$$

which corresponds to the initial state probability distribution $|\psi_i(r)|^2dr$ "reflected" at the wall of the final state potential. The simple harmonic oscillator wave function, Eq. (17), is used for ψ_i. The Morse potentials, Eq. (15), of B and D states are used for the final state. The integral over r of Eq. (18) can then be transformed to an integral over ω by inversion of the Morse potential:

$$r(\omega)=r_e-\frac{1}{\beta}\log\left[1\pm\left(\frac{\hbar\omega-T_e}{D_e}\right)^{1/2}\right] \quad (19)$$

and by keeping only the (+) branch, i.e., the repulsive wall, of the potential. The integration of the transition probability is then carried out numerically in the spectral region of interest according to the desired resolution [typically $\hbar(\omega_{i+1}-\omega_i)=0.005$ eV].

The spectra simulated by the reflection approximation are shown in the inset to Fig. 8, and superposed with the exact solutions in Fig. 9. Quite clearly the approximation is a good representation of the envelope of the stick spectrum. The deviations between these two simulations are within a vibrational energy spacing of the upper state. We conclude that the reflection approximation is valid in this application.

2. Cl:Xe, Br:Xe, and I:Xe absorption spectra

The analysis of the CT absorption spectra of the heavier X:Xe solids will be carried out by extension of the reflection approximation described above. The assumed physical model for these CT states was presented in Sec. I B. The ground states are described by pairwise additive potentials, i.e., the halogen atoms are trapped among equivalent xenons. The excited state potential is described by a radially symmetric, screened Coulomb interaction between the negative halogen ion and the hole. (The self-consistent electrostatic expansion of the field due to a charge among point polarizable atoms is a limiting behavior of this potential presented in Appendix A). The holes are assumed to be centered on any given xenon atom. The probability distributions to be reflected from this attractive potential are the X–Xe radial distribution functions (RDF). The latter are calculated by classical Monte Carlo methods. Since the creation of electron–hole pairs separated by several lattice sites are considered, explicit account of the distance dependence of the transition dipole is taken. Finally, a phenomenological account of the expected strong exciton–phonon coupling is incorporated in the formulation. Several approximations are made for the simulation of spectra.

In what follows, we will first present the formulation and approximations. The radial distribution functions, hence the structures of the ground states, are essential ingredients in the formulation. These are discussed in some detail in Appendix B. The simulated spectra, based on only two adjustable parameters—the interpolaron potential and the distance dependence of the transition dipole—are presented and compared to the experimental spectra in the last section.

a. Solid state reflection approximation. Consider a system consisting of a single substitutionally trapped halogen atom in a xenon solid made of N Xe atoms. For optical charge transfer from the jth Xe atom to the central X atom, the transition probability can be expressed as the Fourier transform of the transition dipole moment time autocorrelation function:

$$P_j(\omega)=\frac{1}{2\pi}\,\mathrm{Re}\left\{\int dt\,e^{i\omega t}\langle\mu(0)\cdot\mu(t)\rangle\right\}. \quad (20)$$

The transition dipole moment is given by

$$\mu(t)=\langle\Psi_f|\mathbf{E}\cdot\hat{\mu}(t)|\Psi_i\rangle, \quad (21)$$

where Ψ_i and Ψ_f are the initial and final states, $\mathbf{E}$ is the optically applied electric field, and the time-dependent dipole moment operator in the Heisenberg representation is

$$\hat{\mu}(t)=e^{i\hat{H}t/\hbar}\hat{\mu}(0)e^{-i\hat{H}t/\hbar}. \quad (22)$$

We assume an exponentially decaying time autocorrelation with decay constant Γ which accounts for the decay of the autocorrelation due to exciton–phonon coupling. Introducing the dependence of the transition dipole moment on the distance to the Xe atom, r_j, the transition probability becomes

$$P_j(\omega)=\mathrm{Re}\left\{\frac{1}{2\pi}\int dt\,e^{i\omega t}|\mu(t=0,r_j)|^2e^{-i\langle\Delta V(r_j)\rangle t/\hbar}e^{-\Gamma t}\right\}, \quad (23)$$

where $\langle\Delta V(r_j)\rangle$ is the difference in final(ionic) and initial (covalent) potential surfaces when Xe atom j is at r_j, averaged over the thermally accessible configurations of the remaining $(N-1)$ Xe atoms. The expression sought for the observed transition probability is the sum of the contributions from all the Xe atoms:

$$P(\omega)=\frac{1}{N}\sum_{j=1}^{N}P_j(\omega). \quad (24)$$

Replacing the summation over the N Xe atoms by an integral over the X–Xe pair distribution function $g_{12}(r)$ yields

$$P(\omega)=4\pi\int dr\,r^2g_{12}(r)|\mu(t=0,r)|^2\times\mathrm{Re}\left\{\frac{1}{2\pi}dt\exp\left[i\left(\omega-\frac{\langle\Delta V(r)\rangle}{\hbar}+i\Gamma\right)t\right]\right\}, \quad (25)$$

where the pair distribution function is normalized to give

$$1=4\pi\int dr\,r^2g_{12}(r). \quad (26)$$

The result of the time integration is a Lorentzian of FWHM $=2\Gamma$, and the transition probability becomes

$$P(\omega)=4\pi\int dr\,r^2g_{12}(r)|\mu(t=0,r)|^2\times\left\{2\Gamma\Big/\left[\left(\omega-\frac{\langle\Delta V(r)\rangle}{\hbar}\right)^2+\Gamma^2\right]\right\}. \quad (27)$$

So far the only assumption made in arriving at Eq. (27) was that of an exponentially dying time correlation. We now introduce, for the various terms in Eq. (27), approximations appropriate to the problem at hand.

(i) First note that the ground state energies accessible at the low temperatures of interest ($T < 50$ K) are negligible in comparison with the observed transition energies (3 to 6 eV). Therefore, the averaged potential difference $\langle \Delta V(r) \rangle$ is dominated by the potential energy of the excited CT state which depends strongly on r. This potential describes the interaction between the oppositely charged polarons. Since the electron is assumed stationary while the hole is mobile, we will refer to this potential as the "hole transport potential" and denote it by $V_{\mathrm{HT}}(r)$. Note that $V_{\mathrm{HT}}(r)$ is the optically accessed potential, hence it is adiabatic with respect to nuclear motions, however it includes electronic polarization. While several forms of this interaction potential can be justified, and perhaps the most appropriate starting point is that given by Fowler,[26] we will opt for the simplest choice by assuming the form

$$V_{\mathrm{HT}}(r) = C_0 - C_1/r \tag{28}$$

which contains two adjustable parameters: an asymptotic energy for infinite separation of the polarons C_0, and an *effective* Coulombic attraction term with coefficient C_1. The asymptote of the potential reflects the self-energies of the hole and electron, given as

$$C_0 = \mathrm{IP(Xe)} - \mathrm{EA(X)} - p^+ - p^-(\mathrm{X}) , \tag{29}$$

where IP(Xe) is the ionization potential of xenon[32] (12.13 eV), EA(X) is the electron affinity of X, p^+ is the self-energy of the hole[44] (2.33 eV), and $p^-(\mathrm{X})$ is the self-energy of the negative ion without lattice relaxation. The potential parameters C_0 and C_1 will be treated as adjustable, and determined from the experimental fits. To a first approximation these values can be obtained from lattice polarization calculations. The detailed electrostatic calculations of the self-energies for the various negative ions, and the electric field, hence C_1, are presented in Appendix A. The calculated values, which are approximate since they do not take into account delocalization, overlap, or exchange terms, are used as a reference point for the interpretation of the experimentally derived parameters.

(ii) Next we assume that the transition dipole is a dying exponential with distance

$$|\mu(t=0,r)|^2 = |\mu_0|^2 e^{-\lambda r} . \tag{30}$$

This is meant to approximate the distance dependence of the overlap between the electron and hole wave functions. Assuming a Wannier type function for the hole, and a strongly localized function for the electron, λ becomes a measure of the extent of delocalization of the hole. As such, λ should be independent of the dopant. This indeed is the case, and the same value of λ will be used to simulate all spectra. We note in passing, that an exponentially decaying transition dipole has also been shown to be valid, by *ab initio* calculations, for the isoiated diatomic exciplex.[40]

(iii) Finally, for the present, we will take the limit of a slowly decaying time correlation function, i.e., $\Gamma \to 0$, so that the time integration in Eq. (25) gives an energy conserving delta function:

$$\mathrm{Re}\left\{\frac{1}{2\pi}\int dt \exp\left[i\left(\omega - \frac{V_{\mathrm{HT}}(r)}{\hbar}\right)\right]t\right\} = \frac{1}{\hbar}\delta[\hbar\omega - V_{\mathrm{HT}}(r)] . \tag{31}$$

Note that this limit can only be realized for the case of a perfectly rigid host. Employing these approximations, and performing the spatial integration, the transition probability becomes

$$P(\omega) = \frac{4\pi}{h}|\mu_0|^2 \int dr\, e^{-\lambda r} g_{12}(r) r^2 \delta[\hbar\omega - V_{\mathrm{HT}}(r)] . \tag{32}$$

Note the similarity between this expression, and the result obtained for the diatomic molecule in the reflection approximation, Eq. (18).

The limit $\Gamma \to 0$ was used above for convenience in the calculation and in the comparison to the diatomic reflection approximation. Properly, the value of Γ reflects the strength of the coupling between the excited state and its surroundings, the exciton–phonon coupling. The effect of a nonzero Γ on the absorption line shapes will be to further broaden them; Eq. (27) shows that mathematically this takes the form of a convolution of the $\Gamma \to 0$ limit spectrum with a Lorentzian of FWHM $= 2\Gamma$.

b. Spectral simulations and comparison to experiment. The excitation spectra that motivated the above formulation were presented in Figs. 3 and 4. Note that prior to annealing of the solids, the spectra are structureless. Upon annealing a well defined structure evolves which shows a reversible dependence upon subsequent heating cycles. In Fig. 10, excitation spectra for Cl, Br, and I doped xenon, recorded at two different temperatures each, are collected. The origins of the spectra for the different halogens have been shifted to match

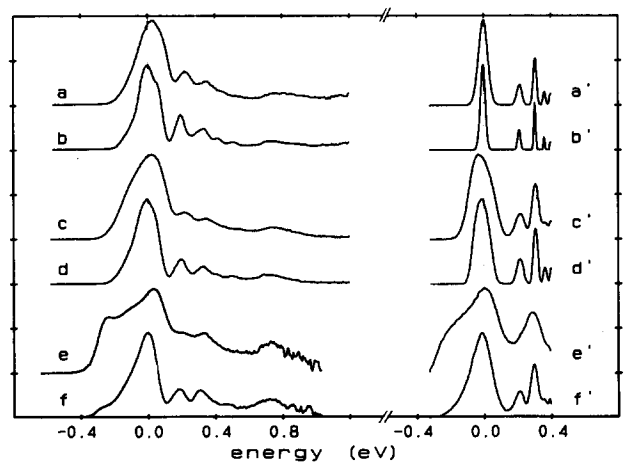

FIG. 10. Observed and simulated X:Xe absorptions in solid Xe. (a) X = I at 50 K, (b) X = I at 12 K, (c) X = Br at 50 K, (d) X = Br at 12 K, (e) X = Cl at 50 K, (f) X = Cl at 12 K. The primed curves are the result of the simulations using the RDFs in Fig. 13. The spectra for each halogen are shifted by the energy of the peak of the observed 12 K absorption.

the first maxima of the low temperature spectra. The observed features are clearly independent of the nature of the halogen (except for the red-most shoulder in Cl which will be discussed), and can therefore be safely ascribed to the host. This structured absorption is presumed to be a direct reflection of the radial distribution of xenons around the impurity site.

The spectra are simulated by the expression for reflection of the RDF from the hole transport potential V_{HT}. The necessary ingredients for the simulations, according to Eq. (32), are the RDFs, which are discussed in some detail in Appendix B; λ, which defines the range of the transition; C_0 and C_1, which define V_{HT} (R). Once these parameters are chosen, the transition probabilities are integrated numerically by an algorithm similar to the one used in the case of XeF.

Once a choice of ground state XeX pair potentials are made (in the present the gas phase pair potentials are used without further modification) the RDF can be simulated for an assumed structure of the solid. Three different structures were used as starting points: fcc, hcp, and random close packed. The spectra could only be reproduced by the fcc structure. The pertinent radial distribution functions are given in Appendix B.

The choice of λ was made to match the relative heights of the first and second absorption peaks in the Br:Xe spectrum; $\lambda = 0.7$ Å^{-1} meets this criterion.

The parameters of V_{HT}, C_0, and C_1 were chosen to match the positions of the observed peaks, i.e., to match the peaks of the RDF (Table VIII) with those of the spectra (Table II). These parameters are collected in Table V. We note that C_0 values have the expected trend, they scale according to the electron affinities of the halogens. From C_0, using Eq. (29), the polarization energies of the halides, $p^-(X)$, can be derived. These derived values are listed in Table V together with the polarization energies [$W_{solid}(X)$] calculated in Appendix A. The derived values are in good agreement with those calculated from the electrostatic model. The values of C_1 necessary to reproduce the spectra range from 3.5 to 3.8 eV Å. These are nearly a factor of 2 smaller than that expected from the electrostatic calculation. There (Appendix A) it was shown that beyond the first nearest neighbor the potential should be well represented as $e^2/\epsilon r$, hence a value of $\sim$6.6 eV Å is to be expected based on a model of point charges.

The factor of 2 difference between the observed value of C_1 and that expected by consideration of the hole transport potential alone in the formation is clearly due to the neglect of the hole kinetic energy within the Coulombic field of the negative ion. (Note that this is correctly accounted in the estimate of C_0 by assuming 2.33 eV for p^+.) A centrifugal force, hence kinetic energy of the hole, is essential to prevent the collapse of the charge pair on the photon absorption time scale. Thus the observed resonances are to the excitonic energies. Since the electron is taken to be of infinite mass, the energies are due to the hole transport energy E_{HT} in which $E = T + V$. For a Coulombic potential, by the virial theorem, $E = -\frac{1}{2}V + V = V/2 = e^2/2\epsilon r$. The above development for the spectral simulation remains valid, however, more properly, V should be replaced by E in Eqs. (23)–(32). The picture is then one of a hole delocalized over xenon shells.

TABLE V. Charge transfer potential parameters.

	Cl	Br	I
C_0 (eV)	4.528	4.873	5.297
C_1 (eV Å)	3.498	3.730	3.807
EA (X) (eV)[a]	3.61	3.36	3.06
p^- (X) (eV)[b]	1.66	1.57	1.44
W_{solid} (X) (eV)[c]	1.11	1.12	···

[a] Reference 32.
[b] Negative ion solvation energies derived from the experimental spectra using Eq. (29).
[c] Negative ion solvation energies calculated from the electrostatic calculation of Appendix A.

The simulated spectra based on the parameters described above are also shown in Fig. 10. A comparison of all the observed and simulated absorption spectra shows that the model can match the positions of the peaks within $\pm$ 0.01 eV. However, there is a systematic overestimate of the energy difference between the first two peaks. We expect that the simulated peak spacings will be more sensitive to the HT potential than to the RDFs, which determine the peak widths and overall shapes. This points to the importance of repulsive terms which would flatten the short range part of the hole transport potential. At short distances the hole transport potential should begin to exhibit some repulsive character, analogous to the diatomic exciplex potential. This aspect has not been incorporated in V_{HT} of Eq. (28). There is qualitative agreement in the trend of decreasing peak widths and increasing resolution of the peaks in the series Cl, Br, and I as expected from the RDFs. The most glaring discrepancy is the overestimate of the intensity of the third peak in the spectra. Note that the third peak corresponds to the first shell of xenons that are screened from the halogen by a completed sphere of nearer neighbors. The simple exponential form chosen for the transition dipole distance dependence is not flexible enough to account for such differences.

There is particularly good agreement between model and experiment in the widths, shapes, and temperature dependence of the peaks in the Cl:Xe spectra. In particular, the red edge of the absorption and its temperature dependence is well reproduced. The red tail is due to charge transfer between a Cl atom and a nearest neighbor Xe upon closest approach in the ground state. The description of the Cl atom–rigid Xe cage potential surface, and the structural interpretation of the features in the X:Xe RDFs given in Appendix B, imply that these closest approaches take place due to motion of the Cl atom into the six wells of the octahedral substitutional cage. In these C_4 sites, the point located midway between the cage center and a second nearest neighbor Xe, corresponds to the octahedral *interstitial* site, however with one of the apex Xe atoms absent. The Cl–Xe distances are small at this site, 3.07 Å at 15 K, and equal to half the lattice parameter. Assuming that V_{HT} derived from the substitutional site also applies for a Cl atom in an octahedral interstitial site leads to the assignment of the small peak on the red tail of the observed Cl:Xe spectra to absorptions involving interstitially trapped Cl atoms. Among these halo-

gens, only Cl can fit in an interstitial site. The absence of this feature in Br and I spectra further corroborates this assignment. The small intensity of this absorption and the absence of other related spectral features is attributed to a small concentration of interstitially trapped Cl atoms after annealing. Note in Fig. 3 it is clear that initially Cl atoms are exclusively trapped at interstitial sites. This is in agreement with molecular dynamical simulations of Cl_2 photodissociation in rare gas clusters in which atomic dissociation products are always seen to be trapped at tight interstitial sites.[45]

The agreement between the widths of observed and simulated spectra is not as good in the Br:Xe case, and much poorer for I:Xe. The widths of the simulated Br:Xe peaks (first peak FWHM = 0.12 eV at 15 K) are smaller than the observed widths (first peak FWHM = 0.16 eV at 15 K). The widths of the simulated I:Xe peaks (first peak FWHM = 0.04 eV at 15 K) are *much* smaller than the observed widths (first peak FWHM = 0.15 eV at 15 K). In addition, splittings are obvious on several of the peaks in the I:Xe spectrum which cannot be explained by the model in which the RDFs are simulated for perfect fcc structures. The simulated spectra were calculated in the limit of zero lattice–exciton coupling, $\Gamma \rightarrow 0$. As long as the broadening due to exciton–lattice coupling is less than the widths due to motion of X atoms, the simulations should be satisfactory. This obviously is the case for Cl. However, in the case of I, in which the atom fits tightly in the substitutional site, it is expected that the polarization modulation by the phonon bath will dominate the linewidths. This effect is however difficult to separate from inhomogeneities in the isolation sites. We will therefore refrain from analysis of the widths. It is however worth speculating that the splittings of the peaks in the I:Xe spectrum indicate the possibility of a distortion in the local lattice structure; the presence of a nearby H atom or a precursor molecule is a likely source of this distortion. In molecular dynamical simulations[13] of HI photodissociation in crystalline xenon, it is observed that the ejected H atom is always immobilized at a nearby tetrahedral interstitial site creating ~ 0.3 Å radial dilation around it. This type of lattice distortion would be sufficient to cause splitting of the RDF peaks.

The weak absorption observed at 0.7 eV to the blue of the main excitation peak is common to all the spectra. The analysis of the F:Xe spectrum pointed out the importance of the ionic potential derived from the spin-excited $Xe^+(^2P_{1/2})$ state in explaining the second excitation maximum there. Hence it is tempting to assign the weak feature in the spectra of the heavier halogens to transitions involving a spin-excited hole. We reject this assignment since the spin–orbit splitting in solid xenon is known to be[13] 1.3 eV, hence outside the range of our experimental spectra. Note, however, that 0.7 eV corresponds to the asymptotes of the hole transport potentials used in the simulations. At this limit, it should be possible to create free holes. Thus, we make the tentative assignment of the weak high energy feature to CT transitions which create ion–free hole pairs. We also predict that photoconductivity experiments in these solids should show a marked increase in conductivity at these excitation energies.

Finally, the inadequacy of the gas phase two-body potentials in describing the many-body ground state surface in the solid phase is manifested in the temperature dependent shift of peak positions. In all cases, the experimental spectra undergo a blue shift upon warmup. This is not observed in the simulated spectra. Refinement of the ground state potentials by an iterative scheme should be possible. However, this is deferred to the future, to studies involving halogen doped crystalline xenon.

V. CONCLUSIONS

We have extended our previous study of the localized CT states in HCl, Cl_2, and Cl doped rare gas solids to complete the series of halogens in solid xenon. The correlation between gas phase $Xe_2^+X^-$ emissions and those observed following near UV excitation of X doped Xe solids demonstrates the generality of the assignment to $Xe_2^+X^-$ as the identity of the lowest CT state of the solid, and confirms the Coulombic binding model for these exciplexes. Moreover, we have established that independent of the excitation energy, *emission is exclusively observed from these localized molecular charge transfer states.* No intermolecular energy transfer is observed among exciplexes, due to the large Stokes shifts in the triatomic emissions; multiply doped solids do not show energy transfer between dissimilar exciplexes, again due to the absence of spectral overlap between emissions and absorptions. Thus *the exciplexic states are truly isolated* in these solids.

Excitation spectra obtained by monitoring the $Xe_2^+X^-$ emissions probe the Franck–Condon accessed CT states of the X doped Xe solids prior to relaxation. In the case of F:Xe solids, the spectra can be simulated as the gas phase diatomic $XeF(B \leftarrow X)$ and $XeF(D \leftarrow X)$ absorption envelopes—shifted and broadened by the polarizable host. Since the Xe···F bond length in the ground state is shorter than that of the excited state, only the repulsive wall of the charge transfer potentials are probed; hence the success of the treatment is not too surprising. In the case of the heavier halogens, in annealed solids, structured excitation spectra are observed. These spectra are simulated with good qualitative agreement by reflection of X–Xe radial distribution functions from an excited state potential of simple Coulombic form. The formulation and assumptions were presented in some detail. The treatment, while approximate, leads to a definite description of the vertically accessed CT states in these systems: a CT exciton in which the electron is localized on the halogen atom (infinite effective mass), and a hole which in the Coulombic field of the negative ion is only partially delocalized (heavy) and therefore assumes the same space as the lattice points of the solid. The charge transfer spectra in these systems therefore offer *a powerful tool for probing the long range interaction between ion and hole in the excited state, and the extended structure of the solid in the ground state.*

The experimentally determined hole transport potential, adiabatic with respect to nuclear coordinates and fully diabatic with respect to electronic coordinates, leads to an asymptotic limit that could be predicted based on known energetics of holes in solid xenon, and self-energies of halogen ions obtained by self-consistent electrostatic calcula-

tions. The potential is soft compared to that of a pair of point charges in the same medium indicating its diabatic nature with respect to electronic coordinates, and the delocalized nature of the hole. Structural information is crucial to the understanding of dynamics in dense media. The local structure in the annealed X/Xe solids is fcc, and qualitatively well reproduced by pairwise summation of the gas phase pair potentials. In the case of Cl doped solids, prior to annealing, the photogenerated atoms are seen to occupy interstitial sites. Upon annealing they interconvert to substitutional. This would first imply that vacancies are present in the solids. More significant is the inference that during the photodissociation process sufficient disorder (local melting) is produced such that nearest neighbor interactions alone control structure, and hence clustering of xenon atoms to the tightest geometry (interstitial geometry) around the impurity ion results. Upon annealing long range order is established, and the lattice cohesion energy dictates the structure—the xenon atoms assume their lattice sites creating the looser substitutional trap sites for the guest atoms. Improvement of experimental spectra is to be expected by resorting to crystalline solids and to lower temperatures (work in progress). This is expected to lead to improvement of derived potentials specifically with respect to the ground state where many-body contributions could in principle be extracted. Improvement of the theoretical formulation, in particular with respect to treatment of intensities would be very useful.

Although *the optically accessed CT states are excitonic* in nature (eigenstates of the extended solid) *emission is only observed from the exciplexic states* (molecular eigenstates). Thus the charge transfer excitons are strongly coupled to the lattice, and self-trap to the molecular configuration, the triatomic xenon halide exciplexes, with near unity quantum yield. This is the more general statement of the four level laser analogy for the photocycle of absorptions and emissions in these systems, which had been previously suggested.[5] The efficiency of the photocycle provides for a very sensitive probe of halogen atom concentrations, and hence of the dissociation of halogen atom precursors. The ease with which even the large diatomic halogens are permanently dissociated points to a different mechanism than direct photodissociation via neutral molecular potentials followed by cage exit of a fragment. The observed power dependences and rates of growth of halogen atom concentrations in solids doped with the molecular halogens, are consistent with a two-photon cooperative mechanism in which the excitation is to the $X^+Xe_2^-$ charge transfer state. We propose that the subsequent ejection of the halogen fragment is accompanied by a concerted rearrangement of the cage atoms which, due to the large polarizability of Xe, are attracted by the dipole of the nascent Xe^+X^- exciplex. This *negative cage effect* aids in squeezing out the halogen fragment, and the cage rearrangement prevents its later return and recombination. Note that cage collapse around the ionic moiety is to be expected to only occur during the period of the accommodation of the excess energy, in the "hot" cage. Otherwise, it was shown in our calculations, in the appendices, that due to the cohesive energy of the lattice, cage collapse around neither halogen atom nor halogen ion is significant. Experiments on photodissociation dynamics in rare gas liquids and crystalline rare gas solids corroborate this interpretation.[7]

The delocalized nature of the optically accessed CT state, and the limited mobility of the hole, suggests an alternate mechanism for the relaxation of the excitonic state; namely the self-trapping of the hole which would lead to charge separation. While a minor channel for relaxation, this process has indeed been observed, and will be characterized in the following paper in which the excitonic dynamics is discussed at greater length.

ACKNOWLEDGMENTS

This research is supported by the United States Air Force Astronautics Laboratory under Contract F04611-87-K-0024. We also gratefully acknowledge the support of early stages of this research by a grant from the Research Corporation.

APPENDIX A

Both in this paper and in subsequent reports, the binding energy of an electron to a halogen atom isolated in RGS is a central issue. The binding energy is defined relative to the bottom of the conduction band and includes contributions from electron affinity of the halogen atom, from the purely electronic polarization of the solid, and from distortion of the lattice due to the presence of the excess charge. Because of the large electron affinities of the halogens (3.0 to 3.6 eV), the electron will be strongly localized on the halide ion, hence "static" approximations[26] to the more general problem of a polaron in RGS are particularly appropriate.

In this spirit we have carried out self-consistent classical electrostatic calculations of the binding energies in solid Xe. We begin with calculations in a rigid solid which yield the contributions from electronic polarization only. These calculations are then extended to include limited, radial deformations around the halide ion in order to estimate the importance of lattice relaxation. The results are summarized in Table VII.

1. Cavity model

The major contribution to the energetic stabilization of an impurity ion in a rare gas solid arises from the polarization of the solid by the ion's electric field. In the simplest approximation, the ion is considered as a nonpolarizable point charge of magnitude q, situated in a spherical cavity of radius r_0 in an infinite homogeneous solid characterized by dielectric constant ϵ. The stabilization energy W_{cavity} is calculated as the difference between the energy densities of the fields in the solid and in vacuum, integrated over the volume of the dielectric:

$$W_{\text{cavity}} = -\tfrac{1}{2}(1 - 1/\epsilon)q^2/r_0. \qquad \text{(A1)}$$

The cavity radius r_0 is not well defined in this model, but "reasonable" stabilizations are calculated for values of r_0 approximately equal to the distance between the ion and its nearest neighbor atoms (see Table VI). The major flaw of this model is the neglect of the anisotropy and distance dependence of the solid's polarizability for small values of the cavity radius. A model that includes explicitly the discrete nature of the solid for short distances from the impurity ion

TABLE VI. Polarization stabilization energies for an ion in a xenon solid ($\epsilon = 2.20$) as given by the cavity model. The smaller radii correspond to the ion–nearest neighbor xenon distances, while the larger radii give the long-range stabilizations for the discrete lattice calculations (see the text).

	Cavity radius (Å)	W_{cavity} (eV)
Substitutional site	4.340	−0.905
	14.39	−0.273
O_h interstitial site	3.069	−1.280
	12.65	−0.310

is presented below; we retain the cavity model to account for the long range polarization of the solid.

2. Rare gas solid

The rare gas solid is assumed to be composed of point polarizable atoms arranged to form an fcc lattice. The values chosen for the atomic polarizability α and the lattice parameter a determine which rare gas solid is being modeled. We will restrict our attention to solid xenon for which[46] $\alpha = 4.04$ Å^3, and[32] $a = 6.138$ Å.

We perform two sets of calculations in which the lone impurity ion occupies either a substitutional vacancy or an octahedral interstitial site in the lattice. The atoms of the lattice are grouped into "shells" according to their distances from the ion. For example, an ion in a substitutional site has 12 xenon atoms in its first shell (nearest neighbors), 6 atoms in the second shell (second neighbors), etc. For the substitutional site calculations we retain the first ten shells, giving a total of 200 atoms; for the interstitial site calculations we keep eight shells, giving 188 atoms. In the following section we will justify truncating the calculations at these limits.

3. Rigid-lattice point-charge electrostatics

The method consists of an iterative process for calculating a self-consistent electric field at the position of each xenon atom. The electric field at atomic position $\mathbf{x}_j$ due to a nonpolarizable impurity ion with charge q is[47]

$$\mathbf{E}_{\text{ion}}(\mathbf{x}_j) = q\mathbf{x}_j/|\mathbf{x}_j - \mathbf{x}_0|^3, \tag{A2}$$

where $\mathbf{x}_0$ is the position of the ion, and j labels the xenon atoms. This value of the electric field is used initially to calculate the induced dipole $\mathbf{p}_j$ at each atomic position:

$$\mathbf{p}_j = \alpha\mathbf{E}_{\text{ion}}(\mathbf{x}_j), \tag{A3}$$

where α is the atomic polarizability. Each of these induced dipoles contributes its own field at position $\mathbf{x}_k$:

$$\mathbf{E}_{\text{dipole}}(\mathbf{x}_k) = [3\hat{\mathbf{n}}(\mathbf{p}_j\cdot\hat{\mathbf{n}}) - \mathbf{p}_j]/|\mathbf{x}_k - \mathbf{x}_j|^3, \tag{A4}$$

where in Eq. (A4) $\mathbf{x}_j$ is the position of the induced dipole and $\hat{\mathbf{n}}$ is the unit vector between $\mathbf{x}_k$ and $\mathbf{x}_j$:

$$\hat{\mathbf{n}} = (\mathbf{x}_k - \mathbf{x}_j)/|\mathbf{x}_k - \mathbf{x}_j|. \tag{A5}$$

The total field at each atomic position is now the sum of the ion's field and the fields of all the other induced dipoles:

$$\mathbf{E}_{\text{total}}(\mathbf{x}_k) = \mathbf{E}_{\text{ion}}(\mathbf{x}_k) + \Sigma_{j\neq k}[\mathbf{E}_{\text{dipole}}(\mathbf{x}_k)]. \tag{A6}$$

The iteration is performed by using the value of the total field to calculate a set of new values for the induced dipoles:

$$\mathbf{p}_k = \alpha\mathbf{E}_{\text{total}}(\mathbf{x}_k) \tag{A7}$$

and using these dipoles to calculate, in turn, a new total electric field.

After each iteration, the values of the electric field and induced dipoles are used to calculate the energy of the new electrostatic configuration. The polarization energy W_{polar} for the system is given by

$$W_{\text{polar}} = \tfrac{1}{2}\sum_k \{\mathbf{p}_k\cdot\mathbf{E}_{\text{total}}(\mathbf{x}_k)\} \tag{A8}$$

and is broken up into a sum of ion–dipole and dipole–dipole energies given by

$$W_{\text{ion-dipole}} = \tfrac{1}{2}\sum_k [\mathbf{p}_k\cdot\mathbf{E}_{\text{ion}}(\mathbf{x}_k)] \tag{A9}$$

and

$$W_{\text{dipole-dipole}} = \tfrac{1}{2}\sum_k\sum_{j\neq k} \{\mathbf{p}_k\cdot\mathbf{E}_{\text{dipole}}(\mathbf{x}_k)\}. \tag{A10}$$

The *rate* of convergence of the calculation is tested by comparing the energies of the configurations before and after each iteration. A convergence parameter is defined as the magnitude of the fractional change in the dipole–dipole energy after each iteration. The dipole–dipole energy is particularly sensitive to the values of the electric field, and both quantities converge simultaneously. We find that for calculations in xenon (both substitutional and interstitial sites) the convergence is exponential with respect to the number of iterations. Since the convergence of the fractional energy change is exponential, the values of the calculated energies also converge exponentially. The *uniqueness* of the final configuration is checked by varying the initial polarizations induced in the xenon atoms. A multiplicative factor in the range of 0.1 to 10.0 was introduced into Eq. (A3); we find that the same final electrostatic configurations are reached independent of the value of this factor. Finally, we confirmed that the radial symmetry of the electric field is preserved throughout the calculation, even though the field is calculated as a sum over *all* the xenon atoms. No explicit use is made of the symmetry of the fcc lattice in order to preserve the generality of the method and applicability to future calculations of less ordered systems.

Figure 11 shows the calculated magnitudes of the electric fields for an ion in a substitutional vacancy (open circles) and in an interstitial site (diamonds). The abscissa corresponds to the distances between the atoms of each shell and the central ion. The lower (dashed) curve is the value of the bare Coulomb field for a point charge in vacuum; the upper (solid) curve is the Coulomb field modified by the dielectric constant of solid xenon:

$$E_{\text{dielectric}}(\mathbf{x}) = q/\epsilon|\mathbf{x} - \mathbf{x}_0|^2. \tag{A11}$$

The calculated field values approach those of the continuum dielectric model for large distances.

Figure 12(a) shows the dependence of the electrostatic stabilization energy for an ion in a substitutional site on the number of atoms used in the calculation. The abscissa n_s corresponds to the number of shells used in the calculation. The calculated polarization energy for the configuration W_{polar} is plotted as the closed diamonds. The remainder of the solid is treated using the cavity model described above with the radius of the cavity given by the distance from the

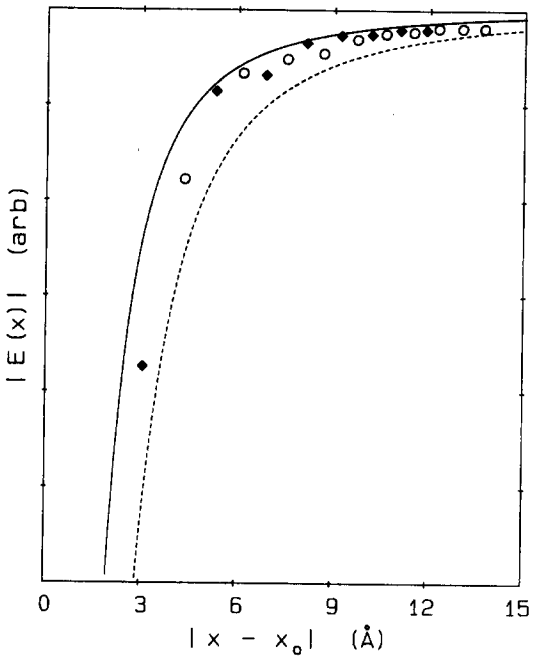

FIG. 11. Magnitude of electric field around an ion in solid xenon (see the text for legend).

ion to the atoms in the $(n_s + 1)$th shell. This contribution W_{cavity} is given by Eq. (A1) and is plotted as the open circles. The total electrostatic stabilization energy W_{electr} is given by the sum of W_{polar} and W_{cavity} and is plotted as the closed triangles. The apparent convergence of the values of W_{electr} justifies the truncation of the calculation at the tenth shell. Figure 12(b) shows an analogous plot of the stabilization energy vs number of shells for an ion in an interstitial site in solid xenon; this calculation has also apparently converged.

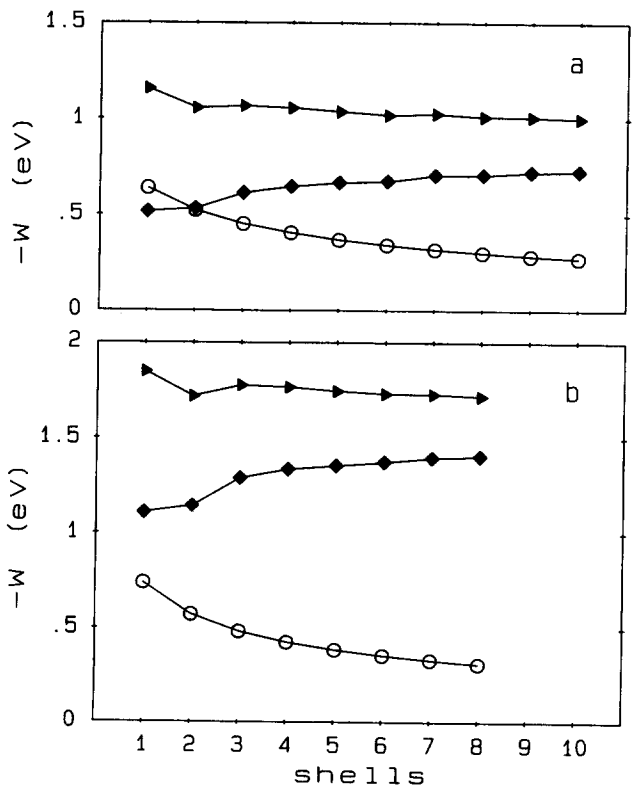

FIG. 12. Dependence of elecrostatic stabilization energy on number of atoms included in calculation (see the text for legend).

4. Rare gas–ion repulsive and dispersive interactions

The values of W_{electr} calculated above represent the electrostatic stabilization energies for a nonpolarizable point charge in two sites of a rigid fcc lattice of xenon atoms. In this section we include repulsive and dispersive interactions between the ion and the xenon atoms in the form of an effective pair potential. In the following section we will extend the calculation to include limited deformations from the fcc lattice structure.

We begin by assuming that the XeX^- pair potential may be written as a sum of three terms: an exponential repulsion term, an attractive charge-induced dipole term, and an attractive dispersion term:

$$V_{XeX^-}(R) = C_1 \exp(-C_2 R) - C_4 R^{-4} - C_6 R^{-6}, \tag{A12}$$

where R is the distance between the X^- ion and the Xe atom. The charge-induced dipole term is already accounted for by the electrostatic calculation described in the previous section. The coefficient C_4 is given in terms of the atomic polarizability of Xe, α, and the ion's charge q as

$$C_4 = \tfrac{1}{2}\alpha q^2 = 29.12 \text{ eV Å}^4. \tag{A13}$$

The remaining coefficients C_1, C_2, and C_6 in Eq. (A12) are evaluated by fitting that expression to an experimentally determined XeX^- potential, after subtraction of the charge-induced dipole term with C_4 given in Eq. (A13). The XeX^- potentials given in Ref. 48 are derived from gaseous ion transport data and are estimated by those authors to be accurate within 10% over the applicable ranges. No potential for the XeI^- system was given due to a lack of available data. We fit the experimental potentials within 15% using the exp-4-6 form. Accordingly, the repulsive and dispersive ion–atom interactions are presented by an effective potential of the form:

$$V_{\text{exp-6}}(R) = C_1 \exp(-C_2 R) - C_6 R^{-6}. \tag{A14}$$

The contribution of these interactions to the stabilization energy is evaluated by summing over all X^-/Xe pairs:

$$W_{\text{exp-6}} = \sum_j V_{\text{exp-6}}(R_j), \tag{A15}$$

where $R_j = |\mathbf{x}_j - \mathbf{x}_0|$ is the distance between the central ion and the jth Xe atom.

The values of the various contributions to the negative ion stabilization energies in an undistorted fcc Xe solid are included in Table VII. In all cases it seems that some distortion of the lattice away from the fcc structure could lower the energy of the ions.

5. Electrostatics with lattice relaxation at 0 K

The motion of Xe atoms away from the initial fcc structure is considered by introducing into the calculation a Xe–Xe potential which is summed over all Xe pairs to determine their contribution to the lattice relaxation energy. Lim-

TABLE VII. Results of lattice electrostatics calculations for undistorted (fcc) and relaxed xenon solid. r_1 and r_2 are the distances from the halide ion to the first- and second- nearest neighbor xenon shells. $W_{\text{ion-dipole}}$, $W_{\text{dipole-dipole}}$, $W_{\text{exp-6}}$, and W_{XeXe} are defined in the text; W_{solid} is the sum of these energies and W_{cavity}. The total binding energy W_{bind} is the sum of W_{solid} and the halogen atoms' electron affinity. All distances are in Å, all energies in eV.

System	r_1	r_2	$W_{\text{ion-dipole}}$	$W_{\text{dipole-dipole}}$	$W_{\text{exp-6}}$	$W_{\text{Xe-Xe}}$	W_{solid}	W_{bind}
Substitutional site								
Br^- fcc	4.340	6.138	−1.0861	0.3569	−0.1177	0	−1.120	−4.48
relaxed	4.260	6.150	−1.1306	0.3764	−0.1253	0.0137	−1.139	−4.50
Cl^- fcc	4.340	6.138	−1.0861	0.3569	−0.1060	0	−1.108	−4.72
relaxed	4.261	6.150	−1.1303	0.3762	−0.1117	0.0135	−1.125	−4.74
F^- fcc	4.340	6.138	−1.0861	0.3569	0.0022	0	−1.000	−4.40
relaxed	4.278	6.152	−1.1200	0.3716	0.0028	0.0075	−1.011	−4.41
O_h interstitial site								
Cl^- fcc	3.069	5.316	−1.8355	0.4919	0.8285	0	−0.826	−4.44
relaxed	3.288	5.309	−1.5593	0.4014	0.2311	0.0915	−1.146	−4.76
F^- fcc	3.069	5.316	−1.8355	0.4919	0.1554	0	−1.499	−4.90
relaxed	3.017	5.316	−1.9131	0.5199	0.1916	0.0049	−1.507	−4.91

ited, radial, distortions for the two nearest shells of Xe atoms around the central ion are considered. Finally, values of minimized energies and geometries for X^- ions in substitutional and interstitial sites in solid xenon are presented.

The Xe(X4) potential of Barker *et al.*[38] which has a well depth of 0.024 33 eV at the equilibrium distance of 4.3634 Å, was used to represent the solid state Xe–Xe interaction. The zeros of energy for both interstitial and substitutional calculations were defined using this potential. For the interstitial case, the zero was taken as the energy of the collection of 188 Xe atoms at their positions in the undistorted fcc lattice. For the substitutional case, the zero was defined as the energy of the collection of 200 atoms surrounding the vacancy at their positions in the undistorted fcc lattice. The energy necessary to create the vacancy and the lattice relaxation energy around the vacancy ($\approx$0.20 and ~ -0.03 eV, respectively) are not included for the sake of comparison with the interstitial case. Experimentally, we expect that such vacancies are already present in the solid when the matrix is deposited and so are readily available for the inclusion of impurities.

Radial movement of the atoms in each shell around the central ion were introduced to measure the effects of lattice relaxation. A complete electrostatic calculation was performed for each new lattice geometry to determine the energy of the configuration. We find that the major contribution to minimization of the energy is realized by motion of the first shell alone. An iterative gradient search method was used to find the minimum energy configuration. Only the two nearest shells were allowed to move in order to mimic the rigidity of the bulk solid, without appealing to periodic boundary conditions which would limit the ion–rare gas dilution. We present the results of our minimized calculations in Table VII.

We note first that for the ions trapped in a substitutional site, the values of W_{solid} are very similar, ~ -1.0 to -1.1 eV; these values compare well with the experimentally determined negative ion self-energies $p^-(X)$ in Table V of the text. Also the effects of lattice relaxation are minor: a contraction of the nearest neighbor xenons of less than 0.1 Å resulting in an additional net stabilization of ~ -0.01 to -0.02 eV. In the case of an interstitially trapped chloride ion the effects of lattice relaxation are pronounced, due mainly to the repulsive Cl^-–Xe interactions; the energy of the relaxed configuration is close to that for a substitutionally trapped Cl^-. The largest stabilization is found for an interstitially trapped F^- ion, ~ -1.5 eV.

APPENDIX B

We use the original Metropolis algorithm[49] for Monte Carlo integration over configuration space to calculate the X–Xe ground state RDFs. Briefly, the method involves the generation of a sequence of configurations of an ensemble of atoms over which the property of interest is averaged, in this case the X–Xe distances. Each new configuration is generated from the previous one by a random displacement of one of the atoms; acceptance is random with a weighting given by the Boltzmann factor of the energy difference between configurations. If the new configuration is not accepted, the old one is kept for the averaging process. Enough configurations are sampled to ensure the accuracy of the integration.

1. Xenon solid

We begin by assuming that the Xe solid can be taken as an fcc Xe crystal. The crystal is modeled by a roughly cubical collection of 108 atoms constituting sections of six (100) planes in the fcc lattice. The atoms form a cell from which a complete fcc lattice can be built by repetitive packing. Periodic boundary conditions are used to mimic the infinite solid. The separation between atoms, and hence the density of the solid, is determined by the lattice parameter a. For Xe at 15 K and 50 K, the use of $a = 6.138$ and 6.176 Å, respectively, simulates the effects of thermal expansion.[50]

The X atom is introduced in place of one of the Xe atoms nearest the center of the cell, and hence in the initial configuration it occupies a substitutional site in an otherwise undistorted fcc lattice. This arrangement accounts for all of the Xe atoms in the first four nearest neighbor shells around the X

atom, however half of the fifth shell Xe atoms are not included. This limits the calculation of the X-Xe RDF to the fourth nearest neighbor shell.

2. Potentials

In evaluating the energy of each configuration, we assume that the ground state potential surface can be described as sums of pairwise interactions. The X–Xe potentials are derived from molecular beam scattering data (see references in Table III), and are expected to be very good descriptions of the gas phase X–Xe interactions. It is not necessarily the case that the same potentials will describe X–Xe interactions in solid Xe. One would expect the gas phase potentials to be adequate if the source of the X–Xe interactions were essentially London forces. However, substantial perturbation is expected in the case of ionic or covalent bonding interactions. Here the unmodified gas phase X–Xe potentials are used for the sake of simplicity in the interpretation of the simulations and comparison with experimental data. The Xe–Xe potential is taken from Ref. 38 and is a good effective pair potential for Xe–Xe interactions in the solid, since the potential parameters are fitted to reproduce solid state data.

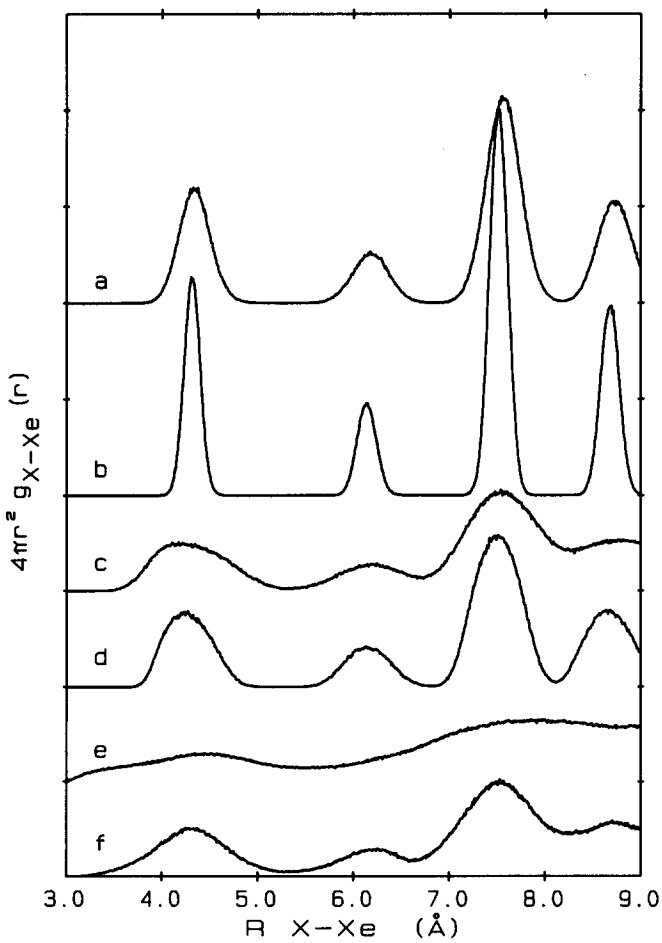

FIG. 13. Calculated X–Xe RDFs for substitutionally trapped X in fcc solid xenon. (a) X = I at 50 K, (b) X = I at 15 K, (c) X = Br at 50 K, (d) X = Br at 15 K, (e) X = Cl at 50 K, (f) X = Cl at 15 K. Table VIII lists the positions and widths of the peaks.

TABLE VIII. X:Xe RDFs. All distances in Å.

	Cl	Br	I	fcc
15 K				
First peak max	4.31	4.24	4.31	4.340
FWHM	0.82	0.61	0.19	
Second peak max	6.22	6.14	6.14	6.138
FWHM	0.74	0.55	0.23	
Third peak max	7.53	7.50	7.51	7.517
FWHM	0.96	0.61	0.23	
Fourth peak max	8.71	8.66	8.69	8.680
FWHM	···	0.58	0.22	
Fifth peak max[a]	···	9.58	9.65	9.705
50 K				
First peak max	4.37	4.25	4.32	4.367
FWHM	1.57	0.84	0.37	
Second peak max	6.25	6.16	6.16	6.176
FWHM	1.07	0.70	0.40	
Third peak max	···	7.53	7.51	7.564
FWHM	···	0.80	0.42	

[a] Note fifth nearest neighbor shell is incomplete in the simulation.

3. Calculation of RDFs

By monitoring during the calculation the values of and fluctuations in the total energy and positions of the atoms in the ensemble, one can follow the system's approach to equilibrium. The process of accumulating the averages is postponed until memory of the initial configuration is lost. With a 50% acceptance rate of new configurations, averaging the RDF can be started after ignoring 10 000 configurations. The RDF is calculated by rounding the X–Xe distances to the nearest 0.01 Å and binning the contributions. Further iterations are performed until a satisfactory S/N ratio is achieved. We accumulated 2×10^6 averages in most cases (4×10^6 for the high temperature Cl–Xe RDF) although fewer averages were in principle needed in the I–Xe case where the peak are narrower.

Figure 13 shows the X–Xe RDFs (actually $4\pi r^2 g_{12}$) calculated for Cl, Br, and I–Xe at 15 and 50 K. The curves are normalized to preserve the areas under the peaks. The peak maxima and widths are listed in Table VIII. We make three simple observations:

(1) The peaks are centered at the fcc nearest neighbor distances.

(2) The widths (FWHM) of the peaks increase in the order Cl–Xe > Br–Xe > I–Xe.

(3) All peaks broaden and shift to higher separations at the higher temperature.

The first observation implies that the lattice is not substantially distorted by the presence of the halogen atom. This is reasonable since the well depths for the X–Xe potentials are comparable to the Xe–Xe well depth. Moreover, it implies that the probability distribution for the X atom position is centered on the substitutional site.

The second observation taken with the first indicates that the major contribution to the widths of the RDF peaks is due to motion of the X atom in a well defined substitutional cage, with the smaller halogen atoms having a greater

range of motion. Consideration of the potential surface generated by moving a Cl atom in a rigid fcc lattice of Xe atoms (see Fig. 15 in I) shows a minimum at the center of the substitutional cage with the potential essentially flat as far as ≈ 1.0 Å from the center. For Cl this is due to cancellation of the attractive parts of the Cl–Xe pair potentials by opposing nearest neighbor Xe atoms. In the case of Br–Xe, the minimum of the pair potential is also smaller than the nearest neighbor distance in solid Xe, hence some flattening of the minimum of the cage potential surface is expected, but not as much as for Cl. The pair potential for I–Xe is very similar to the Xe–Xe potential and the mass of I is close to the mass of Xe so the I atom finds itself in a fairly tight and restricted site, behaving much as another Xe atom would.

A measure of the sensitivity of the calculated X–Xe RDFs to the pair potentials used is given by the following example. If the gas phase Cl–Xe potential is replaced by a Lennard-Jones potential of the same well depth and minimum separation, a very different potential surface is realized. The lack of long range attraction in the LJ pair potential causes the minimum of the potential surface to move from the cage center to the edge or wall of the cage. In fact, six minima are created, aligned with the C_4 axes of the octahedral cage. The resulting Cl atom probability distribution no longer has a maximum at the cage center, rather the Cl atom will hug the cage wall, moving between the minima. This asymmetry introduces additional structure in the Cl–Xe RDF, by splitting the contributions from each nearest neighbor shell into three peaks.

[1]M. E. Fajardo and V. A. Apkarian, J. Chem. Phys. **85**, 5660 (1986).
[2]For a rigorous discussion of cooperative photoabsorptions see, (a) D.L. Andrews and M. J. Harlow, J. Chem. Phys. **78**, 1088 (1983); **80**, 4753 (1984); D. L. Andrews and K. P. Hopkins, *ibid.* **86**, 2453 (1987); (b) I. Last, Y. S. Kim, and T. F. George, Chem. Phys. Lett. **138**, 225 (1987).
[3]Y. C. Yu, D. W. Setser, and H. Horiguchi, J. Phys. Chem. **87**, 2209 (1983); J. K. Ku, G. Inoue, and D. W. Setser, *ibid.* **87**, 2989 (1983); D. W. Setser and J. K. Ku, in *Photophysics and Photochemistry Above 6eV*, edited by F. Lahmani (Elsevier, New York, 1985), p. 621.
[4]M. Boivineau, J. LeCalve, M. C. Castex, and C. Jouvet, Chem. Phys. Lett. **128**, 528 (1986); J. Chem. Phys. **84**, 4712 (1986); C. Jouvet, M. Boivineau, M. C. Duval, and B. Soep, J. Phys. Chem. **91**, 5416 (1987).
[5]M. E. Fajardo and V. A. Apkarian, Chem. Phys. Lett. **134**, 51 (1987).
[6](a) L. Wiedeman, M. E. Fajardo, and V. A. Apkarian, Chem. Phys. Lett. **134**, 55 (1987); Proceedings of IQEC, Baltimore, 1987, PD-16; (b) F. Okada, L. Wiedeman, and V. A. Apkarian, Chem. Phys. Lett. (in press).
[7]M. E. Fajardo, R. Withnall, J. Feld, F. Okada, W. Lawrence, L. Wiedeman, and V. A. Apkarian, Laser Chem. (in press).
[8]V. E. Bondybey and C. Fletcher, J. Chem. Phys. **64**, 3615 (1976).
[9]V. E. Bondybey and L. E. Brus, J. Chem. Phys. **64**, 3724 (1976).
[10]V. E. Bondybey, S. S. Bearder, and C. Fletcher, J. Chem. Phys. **64**, 5243 (1976).
[11](a) L. E. Brus and V. E. Bondybey, J. Chem. Phys. **65**, 71 (1976); Chem. Phys. Lett. **36**, 252 (1975).
[12]B. S. Ault and L. Andrews, J. Chem. Phys. **10**, 4192 (1976).
[13]R. Alimi, R. B. Gerber, and V. A. Apkarian, J. Chem. Phys. **89**, 174 (1988).
[14]M. E. Fajardo, V. A. Apkarian, A. Moustakas, H. Krueger, and E. Weitz, J. Phys. Chem. **92**, 357 (1987).
[15]N. Schwentner, E. Koch, and J. Jortner, *Electronic Excitations in Condensed Rare Gases*, Springer Tract in Modern Physics, Vol. 107 (Springer, New York, 1985).
[16]I. Ya. Fugol, Adv. Phys. **27**, 1 (1978).
[17]J. Frenkel, Phys. Rev. **37**, 1276 (1931).
[18]G. Wannier, Phys. Rev. **52**, 191 (1937).
[19]D. Pudewill, F. J. Himpsel, V. Saile, N. Schwentner, M. Skibowski, and E. E. Koch, Phys. Status Solidi B **74**, 485 (1976); D. Pudewill, F. J. Himpsel, V. Saile, N. Schwentner, M. Skibowski, E. E. Koch, and J. Jortner, J. Chem. Phys. **65**, 5226 (1976).
[20]M. Chergui, N. Schwentner, and W. Bohmer, J. Chem. Phys. **85**, 2472 (1986), and references therein.
[21]I. Last and T. F. George, J. Chem. Phys. **86**, 3787 (1987).
[22]I. Last and T. F. George, J. Chem. Phys. **87**, 1183 (1987).
[23]I. Last, T. F. George, M. E. Fajardo, and V.A. Apkarian, J. Chem. Phys. **87**, 5917 (1987).
[24]I. Last, Y. S. Kim, and T. F. George, Chem. Phys. Lett. **138**, 225 (1987).
[25]See for example, W. A. Harrison, *Solid State Theory* (Dover, New York, 1979).
[26]W. B. Fowler, Phys. Rev. **151**, 657 (1966).
[27]L. Wiedeman, M. E. Fajardo, and V. A. Apkarian, J. Phys. Chem. **92**, 342 (1988).
[28]D. L. Huestis, G. Marowsky, and F. K. Tittel, *Excimer Lasers*, edited by Ch. K. Rhodes, Topics in Applied Physics, Vol. 30 (Springer, New York, 1984).
[29]A. W. McCown and J. G. Eden, J. Chem. Phys. **81**, 2933 (1984).
[30]A. Perrone, A. Luches, and A. Giannattasio, Opt. Commun. **53**, 95 (1985).
[31]D. C. McKean, Spectrochim. Acta Part A **23**, 2405 (1967).
[32]C. Kittel, *Introduction to Solid State Physics*, 5th ed. (Wiley, New York, 1976).
[33]Th. Forster, Ann. Phys. **2**, 55 (1948); D. L. Dexter, J. Chem. Phys. **21**, 836 (1953).
[34]H. Okabe, *Photochemistry of Small Molecules* (Wiley, New York, 1978).
[35]C. H. Becker, P. Casavecchia, and Y. T. Lee, J. Chem. Phys. **68**, 5187 (1978).
[36]C. H. Becker, J. J. Valentini, P. Casavecchia, S. J. Sibener, and Y. T. Lee, Chem. Phys. Lett. **61**, 1 (1979).
[37]P. Casavecchia, G. He, R. K. Sparks, and Y. T. Lee, J. Chem. Phys. **75**, 710 (1981); **77**, 1878 (1982).
[38]J. A. Barker, in *Rare Gas Solids Vol. I*, edited by M. L. Klein and J. A. Venables (Academic, New York, 1976).
[39]P. C. Tellinghuisen, J. Tellinghuisen, J. A. Coxon, J. E. Velasco, and D. W. Setser, J. Chem. Phys. **68**, 5187 (1978); A. L. Smith and P. C. Kobrinsky, J. Mol. Spectrosc. **69**, 1 (1978).
[40]P. J. Hay and T. H. Dunning, Jr., J. Chem. Phys. **69**, 2209 (1978).
[41]J. W. Cooley, Math. Computation XV, 363 (1961); see also J. K. Cashion, J. Chem. Phys. **39**, 1872 (1963).
[42]J. Goodman and L. E. Brus, J. Chem. Phys. **65**, 3808 (1976).
[43]See, for example, G. Herzberg, *Molecular Spectra and Molecular Structure I. Spectra of Diatomic Molecules* (Van Nostrand, New York, 1950).
[44]B. Sonntag, in *Rare Gas Solids Vol. II*, edited by M. L. Klein and J. A. Venables (Academic, New York, 1977), see table on p. 1100.
[45]R. Alimi, A. Brokman, and R.B. Gerber, in *Stochasticity and Intramolecular Distribution of Energy*, edited by R. LeFebvre and S. Mukamel (Reidel, Dordrecht, 1987).
[46]A. Dalgarno and A.E. Kingston, Proc. R. Soc. London Ser. A **259**, 424 (1961).
[47]J. D. Jackson, *Classical Electrodynamics* (Wiley, New York, 1975).
[48]C. C. Kirkpatrick and L. A. Viehland, Chem. Phys. **98**, 221 (1985).
[49]N. Metropolis, A. W. Rosenbluth, M. N. Rosenbluth, A. H. Teller, and E. Teller, J. Chem. Phys. **21**, 1087 (1953).
[50]C. R. Tilford and C. A. Swenson, Phys. Rev. B **5**, 719 (1972).